

RESEARCH ARTICLE

10.1029/2018JC014435

Key Points:

- Kangerdlugssuaq Glacier terminus is regularly exposed to an oceanic heating rate of 0.5 TW during winter
- Wind forcing frequency is a crucial parameter in determining magnitude of heat exchange
- Vertical mixing enhances buoyancy-driven overturning circulation

Supporting Information:

- Supporting Information S1
- Movie S1

Correspondence to:

N. J. Fraser,
neil.fraser@sams.ac.uk

Citation:

Fraser, N. J., Inall, M. E., Magaldi, M. G., Haine, T. W. N., & Jones, S. C. (2018). Wintertime fjord-shelf interaction and ice sheet melting in southeast Greenland. *Journal of Geophysical Research: Oceans*, 123, 9156–9177. <https://doi.org/10.1029/2018JC014435>

Received 1 AUG 2018

Accepted 26 NOV 2018

Accepted article online 5 DEC 2018

Published online 15 DEC 2018

Wintertime Fjord-Shelf Interaction and Ice Sheet Melting in Southeast Greenland

Neil J. Fraser^{1,2} , Mark E. Inall^{1,2} , Marcello G. Magaldi^{3,4} , Thomas W. N. Haine³ , and Sam C. Jones¹ 

¹The Scottish Association for Marine Science (SAMS), Scottish Marine Institute, Oban, UK, ²The Department of Geosciences, University of Edinburgh, Grant Institute, Edinburgh, UK, ³Department of Earth and Planetary Sciences, The Johns Hopkins University, Baltimore, MD, USA, ⁴Istituto di Scienze Marine, S.S. di Lerici, Consiglio Nazionale delle Ricerche, Forte Santa Teresa, Pozzuolo di Lerici, SP, Italy

Abstract A realistic numerical model was constructed to simulate the oceanic conditions and circulation in a large southeast Greenland fjord (Kangerdlugssuaq) and the adjacent shelf sea region during winter 2007–2008. The major outlet glaciers in this region recently destabilized, contributing to sea level rise and ocean freshening, with increased oceanic heating a probable trigger. It is not apparent a priori whether the fjord dynamics will be influenced by rotational effects, as the fjord width is comparable to the internal Rossby radius. The modeled currents, however, describe a highly three-dimensional system, where rotational effects are of order-one importance. Along-shelf wind events drive a rapid baroclinic exchange, mediated by coastally trapped waves, which propagate from the shelf to the glacier terminus along the right-hand boundary of the fjord. The terminus was regularly exposed to around 0.5 TW of heating over the winter season. Wave energy dissipation provoked vertical mixing, generating a buoyancy flux which strengthened overturning. The coastally trapped waves also acted to strengthen the cyclonic mean flow via Stokes' drift. Although the outgoing wave was less energetic and located at the opposite sidewall, the fjord did exhibit a resonant response, suggesting that fjords of this scale can also exhibit two-dimensional dynamics. Long periods of moderate wind stress greatly enhanced the cross-shelf delivery of heat toward the fjord, in comparison to stronger events over short intervals. This suggests that the timescale over which the shelf wind field varies is a key parameter in dictating wintertime heat delivery from the ocean to the ice sheet.

Plain Language Summary A computer simulation of the ocean around Greenland was used to study the movement of water in and out of a large fjord. This is important because warm water that gets into the fjord may come into contact with the Greenland Ice Sheet and cause it to melt. The simulation indicates that a significant amount of warm water comes into contact with the ice during the winter. This was previously difficult to measure because of the difficulties in taking direct measurements of the water during the Greenland winter.

1. Introduction

Recent reduction in the mass of the Greenland Ice Sheet (GrIS) has been most profound near its edge, indicative of ocean triggered melting (Nick et al., 2009; Rignot & Kanagaratnam, 2006). Coastal water temperature has increased contemporaneously (Khan et al., 2014; Straneo et al., 2013); however, direct contact between the ocean and the GrIS is limited to glacier termini, which are typically located within Greenland's fjords. A thorough understanding of the exchange flows between these fjords and the continental shelf is therefore critical for quantifying the ocean's impact on the GrIS.

One of the most acutely affected glaciers in the previous two decades is Kangerdlugssuaq Glacier (KG), which terminates at Kangerdlugssuaq Fjord (KF), and is one of the major outlet glaciers of southeast Greenland. KG destabilized in 2004–2005, when the rate of discharge suddenly doubled (Bevan et al., 2012), and again in 2016–2017 (Suzanne Bevan, 2018, personal communication, 20 April), with re-advance and slowing generally exhibited in the interim period (Khan et al., 2014). KF is of length $L \sim 80$ km and width $W \sim 6$ –8 km with a maximum depth of around 900 m and a sill depth of around 500 m. At the mouth, where it widens to around 20 km, the fjord meets the north end of Kangerdlugssuaq Trough (KT), a 600-m-deep cross shelf channel (Figure 1).

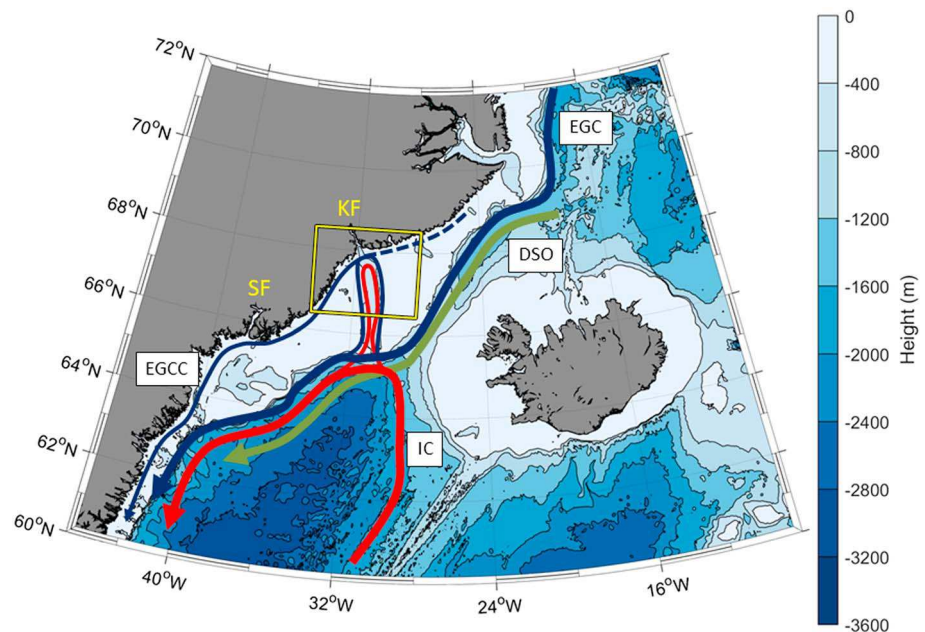


Figure 1. Bathymetry of southeast Greenland seas, with the locations of KF and SF indicated, along with the pathways of the IC, EGC, EGCC, and Denmark Strait Overflow (DSO) and the model domain shown in yellow.

KT is a known pathway for ocean waters from the Irminger Sea (Gelderloos et al., 2017) and intersects the shelf break at its southern end. Here Atlantic Water (AW, conservative temperature (Θ) ~ 4.5 – 6.5°C , absolute salinity (S_A) ~ 34.9 – 35.2 g/kg) flows from east to west in a branch of the North Atlantic Current known as the Irminger Current (IC). A second, seasonal pathway for IC water toward KF is north through the Denmark Strait and across the shelf, leading to a warmer AW layer in winter than in summer (Gelderloos et al., 2017). South of the Denmark Strait, the IC is joined by the East Greenland Current (EGC), which transports Polar Water (PW, $\Theta < 0^\circ\text{C}$, $\sigma_\theta < 27.70$) from the Arctic Ocean. Alongside the EGC, the East Greenland Coastal Current (EGCC) transports PW southward close to the coast. Dense bottom water, termed Denmark Strait Overflow Water (DSOW, $\Theta < 0^\circ\text{C}$, $34.9 < S_A < 35.2$ g/kg, $\sigma_\theta \geq 27.8$), also enters the region here, released over the Denmark Strait sill in periodic boluses (Koszalka et al., 2013).

Due to seasonal sea ice cover, observations of KF hydrography and circulation are biased toward the summer months, when freshwater runoff is strongest, and there is hence a relatively large literature on the buoyancy-driven circulation in Greenland fjords (Carroll et al., 2016; Cowton et al., 2015; Sciascia et al., 2013). A recent study by Moon et al. (2017) highlighted the importance of subsurface iceberg melt as a freshwater source in major SE Greenland fjords. This is also seen in Inall et al. (2014), where the large residual heat loss from PW is associated with iceberg melting within KF. In winter, when runoff is at a minimum, other factors likely play a primary role in driving circulation. Results from Sermilik Fjord (SF; Jackson et al., 2014; Jackson & Straneo, 2016; Sciascia et al., 2014; Straneo et al., 2010; Sutherland, Straneo, et al., 2014), a similarly sized neighbour to KF, indicate that intermediary circulation, a rapid baroclinic exchange regime triggered by along-shelf (with shore to the right) barrier winds, is a significant driver of fjord-shelf exchange. Enhanced wind stress drives coastward flow in the Ekman layer resulting in downwelling of the pycnocline, followed by upwelling once the wind relaxes. In an idealized modeling study into barrier wind forcing of the KF/KT system under winter climatological conditions, Fraser and Inall, (2018; hereafter FI18) see baroclinic exchange flows generated as the displacement of the pycnocline propagates in fjord as a subinertial internal wave. As barrier wind events occur predominantly in the winter months (Harden et al., 2011), the capacity for this mechanism to draw warm ocean waters into contact with glacier termini remains uncertain. Modeling studies of KF (Cowton et al., 2016) and SF (Sciascia et al., 2014) have found that, while intermediary circulation provokes a rapid baroclinic exchange, heat delivery to the glacier is small in comparison with values recorded during summer simulations (Cowton et al., 2015; Sciascia et al., 2014) and field campaigns (Inall et al., 2014; Sutherland, Straneo, et al., 2014). Spall et al. (2017) showed that along-fjord katabatic winds, known as *pitraqs*, can also drive significant exchange.

Two-dimensional overturning regimes, driven by either runoff or shelf exchange, have been the main focus in previous studies of circulation in KF and SF. However, recent observational (Inall et al., 2014; Sutherland, Roth, et al., 2014) and modeling (FI18) studies have indicated these fjords have the capacity for significant lateral velocity variability and recirculation. Carroll et al. (2017) saw a highly three-dimensional flow field develop in idealized broad fjord simulations forced by tides and freshwater input. The modeling study by FI18 found that horizontally sheared, geostrophically balanced flows dominate the mean wintertime circulation in KF and facilitate exchange, with the inflowing (outflowing) currents residing against the right-hand (left-hand) boundary looking into the fjord. Furthermore, the subinertial internal waves, which drive intermediary circulation, were coastal trapped waves (CTWs), with maximum amplitude against the eastern sidewall while propagating up-fjord. Similar three-dimensional internal waves were the focus of a recent combined numerical and analytical study by Jackson et al. (2018), who made significant progress in characterizing their behaviour and influence on exchange. Such cross-fjord variability is only prominent in fjords wider than the internal Rossby radius of deformation, L_R . KF is approximately 6 km across, a width comparable with the Rossby radius of deformation of 8 km estimated under summer conditions (Inall et al., 2014; Sutherland, Straneo, et al., 2014) and which could be even smaller under winter conditions. The potential for a three-dimensional flow field inside KF introduces complexity to the current understanding, and the implications for fjord-shelf heat exchange are not fully understood.

As well as inducing a dynamical response, barrier winds have been found to make enduring changes to the water column structure in the fjord mouth with considerable implications for subsequent exchange. FI18 found that simulations forced with wind events exhibited greatly enhanced vertical mixing in the fjord mouth due to subinertial internal wave activity. Transport in KT was also enhanced by barrier wind forcing, and the extent to which cyclonic circulation in KT penetrated the fjord mouth was increased. Together these factors acted to weaken the stratification in the fjord mouth and introduce a more shelf-like water column structure there, an artifact which remained after the dynamical response to wind forcing (i.e. internal wave activity) had decayed. At a later time, dense bottom waters circulating in KT were able to breach the KF sill and cause a deep water renewal event in the fjord, reminiscent of observations of DSOW within KF (Inall et al., 2014). In model runs where prevailing winds were held constant (without barrier wind events), the mouth, like the KF interior, remained strongly stratified due to the freshening influence of the glacier front, and was resilient to deep-layer exchange with KT.

In this study, we use an adapted version of the model presented in FI18 to study the circulation and exchange in KF during December, January, and February (DJF) of 2007–2008. While FI18 focused on isolating the effect of barrier wind events against a backdrop of winter climatological conditions through the use of a control run, here we look to place their influence in the context of a realistic reconstruction of a winter season. We focus primarily on shelf exchange processes, with the aim of definitively answering the question, “Is there potential for significant wintertime heat exchange between shelf and fjord?”. The model is equipped with a parametrization of the KG glacier front (a heat sink and freshwater source), which generates output variables for glacial melt rates (Cowton et al., 2015). We therefore look for links between glacial melt and various potential drivers of circulation, particularly wind forcing on the shelf.

2. Methods

The model used was the MIT general circulation model, which solves the Boussinesq equations of motion using the finite volume method (MITgcm, Marshall et al., 1997). In this study we also employed the hydrostatic approximation. Integration was performed by the ARCHER UK National Supercomputing Service (<http://www.archer.ac.uk>). The model grid and bathymetry was constructed exactly as described in FI18 and so is only briefly outlined here.

The model domain covers 66.38–68.5°N, 34.59–28.05°W (Figure 2). It captured KF with a horizontal resolution of 360 m and a vertical resolution of 10 m. The grid spacing increased toward the southern, eastern and western boundaries, so that the resolution on the shelf was relatively coarse with a maximum value of 4 km in the southeast and southwest corners. Bathymetry for the shelf region was extracted from the 30-arcsecond International Bathymetric Chart of the Arctic Ocean (IBCAO). Bathymetry for the fjord interior was collected using a swath on the cruise JR106b to KF (Dowdeswell, 2004). An idealized vertical ice front was placed at the northern boundary of the domain, south of the true KG terminus location, as in FI18. Initial and boundary conditions were generated exactly using output from the model presented in Gelderloos et al. (2017), which

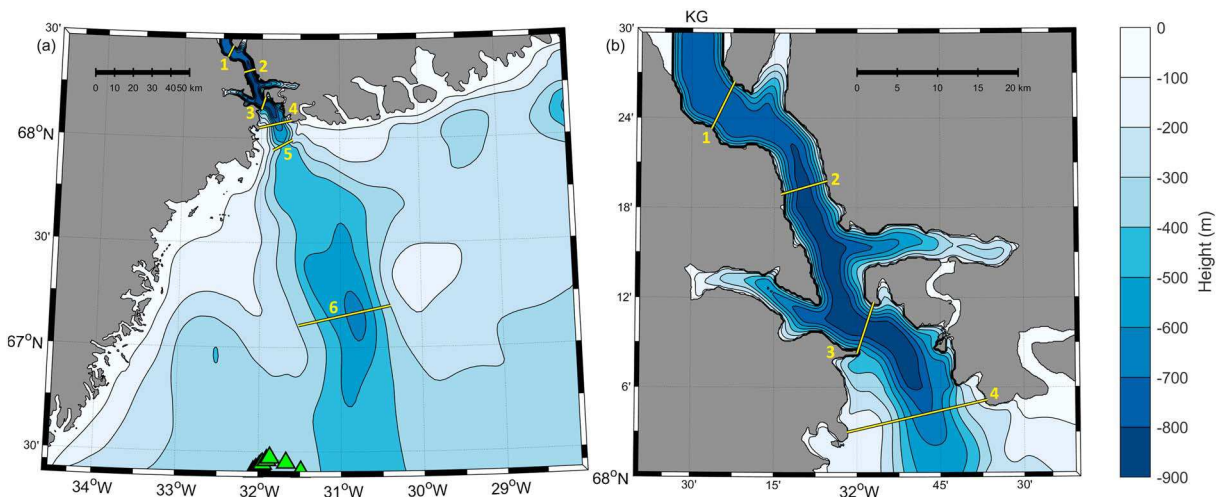


Figure 2. (a) Main model bathymetry, alongside (b) a zoom of the KF interior. Cross-fjord sections are shown and numbered in yellow. Green triangles show the dive locations of an instrumented seal in January 2005, used here for model validation. The modeled location of KG is indicated outside the northern boundary of the right-hand panel.

was used to simulate the wider Irminger Sea region for one year beginning 1 June 2007. The availability of this high-resolution forcing data was our motivation for selecting that particular winter for hindcasting. At material boundaries, no-slip conditions were applied at cell bottoms and free-slip conditions were applied at sidewalls.

Wind and air-sea heat flux data were obtained from ERA-Interim 6-hourly and daily reanalysis products (Dee et al., 2011), respectively. Wind stress fields were calculated using the formula from Large and Pond (1981), which were then modified off-line to reflect local sea ice cover, as described in F118, using temporally varying sea ice concentration data obtained from the National Snow and Ice Data Centre (NSIDC). ERA-Interim wind fields have been shown to resolve high-frequency katabatic winds in SE Greenland fjords (Oltmanns et al., 2014), giving confidence that this product is able to adequately capture near-shore wind processes.

The MITgcm iceplume package (Cowton et al., 2015) was employed to incorporate the dynamical and thermodynamical effects of ice-sea interaction at the idealized KG terminus. The package facilitates prescribed subglacial runoff, analytically solves the plume equations from Jenkins (2011), and calculates local melting as a function of the temperature of the adjacent grid cells according to Holland and Jenkins (1999). A minimum background velocity of 0.02 m/s was applied across the ice face (Cowton et al., 2015). Such a parametrization eliminates the necessity to run the model in nonhydrostatic mode by distributing resultant water masses at the level of neutral buoyancy. We took advantage of the output variables for glacial melt rates provided by the iceplume package as an opportunity to study correlations between glacial melt and fjord-shelf exchange forcings. However, as we later discuss, the package was designed to describe the influence of the ice on the water, not vice versa, so we are cautious when interpreting variables related to glacier dynamics.

We employed the MITgcm implementation of the κ -Profile Parametrization (KPP), introduced by Large et al. (1994), which calculates the vertical mixing coefficient as a function of the bulk Richardson number in the mixed layer and as a function of both the local gradient Richardson number and parametrized double diffusion in the ocean interior, where a constant is also added to represent internal wave breaking (Large et al., 1994). We used the Leith biharmonic scheme (Leith, 1996) to parametrize horizontal viscosity, with nondimensional tuning coefficient $\Lambda_4 = 1$ (Fox-Kemper & Menemenlis, 2008).

As the model by Gelderloos et al. (2017) was not of sufficient resolution to include KF, the initial conditions within the fjord were horizontally extrapolated from the shelf. A 100-day spin-up period was then carried out, with some runoff ($100 \text{ m}^3/\text{s}$) prescribed evenly along the KG grounding line during the initial 60 days in order to allow an overturning circulation to develop within the fjord. This overturning then settled into a wintertime regime during the 40 days of spin up without runoff, sustained only by positive meltwater feedbacks. Wind and boundary forcing were held constant at 1 December values during this period. The model was then integrated forward using dynamic forcing fields for 91 days, the duration of DJF 2007–2008, with a time step of 5 s.

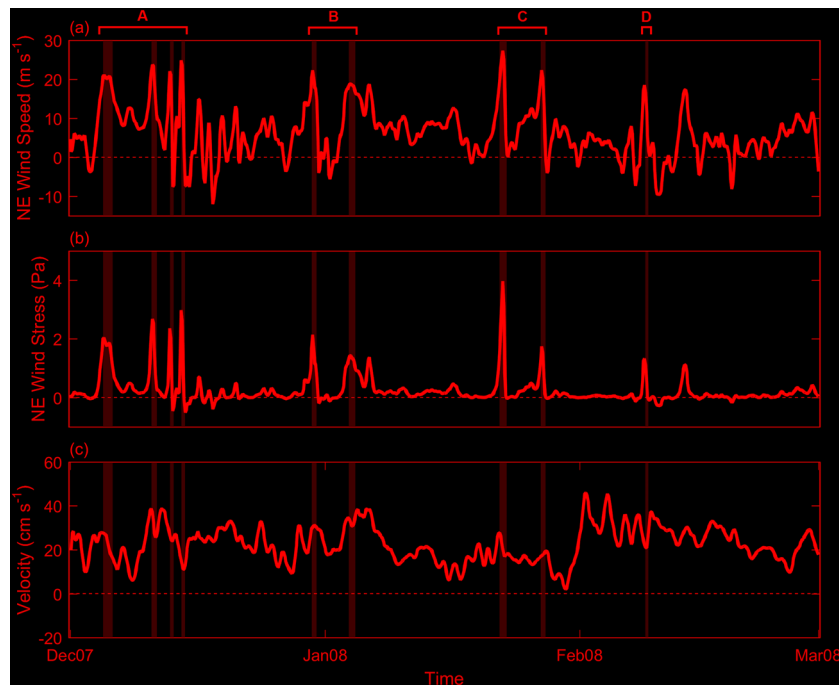


Figure 3. (a) Northeasterly component of wind speed (i.e., the component directed SW) over the deepest point in KT (center of Section 6). (b) Northeasterly component of wind stress over the deepest point in KT. (c) Meridional velocity at the southern boundary taken from the core of the inflow into KT, defined as the region where the mean flow exceeded 20 cm/s. The grayed-out regions denote periods considered barrier wind events by Harden et al. (2011), with wind event clusters labels at the top of the figure.

Harden et al. (2011) define a barrier wind event as wind blowing from the northeasterly quadrant, exceeding 20 m/s, and being distinct in time from other such events by 24 hr or more. According to this definition, nine barrier wind events occurred on the shelf outside KF in DJF 2007–2008, and their occurrences are shown in Figure 3a alongside northeasterly component of wind speed (note that this does not necessarily reflect the Harden et al., 2011, definition threshold). The corresponding wind stress, which is usually quadratic in wind speed but becomes cubic when the wind exceeds 11 m/s (Large & Pond, 1981), is shown in Figure 3b. Barrier wind events occurred less frequently during DJF 2007–2008 than is typical during DJF, with the number ranging from 7 to 20 during 1989–2008 (Harden et al., 2011). Events were generally clustered in time, with four events taking place in early December (hereafter Cluster A), two around the start of January (Cluster B), two toward the end of January (Cluster C), and one in mid-February (Cluster D). Two of the wind events, the first in December and first in January, coincided with prolonged periods of strong northeasterly wind stress, and were hence characteristically different to the shorter peaks seen at other times. Both air and subsurface water temperatures were anomalously high in comparison with the 1981–2012 mean, though consistent with other years since 2000 (Khan et al., 2014). Meridional velocity into KT at the southern boundary is also an important external driver of dynamical variability and is shown in Figure 3c. Barrier wind events regularly coincided with enhanced inflow into the model domain, likely due to the intensification of barotropic currents on the shelf by along-shore wind stress as described in Nilsen et al. (2016). Notable exceptions arise in late January and early February, however, when enhanced inflow did not coincide with wind events, indicating that other factors also influence inflow variability.

3. Results and Analysis

We compared model diagnostics to various in situ measurements in order to gauge model realism. With wintertime observations of the region scarce, no such data was available from within the model domain during the period of study. The vertical temperature structure at 200–300 m depth (Figure 4, Sections 1–3) agrees well with the mooring record by Jackson et al. (2014) in 2009–2010. We also utilized summertime observations from within KF, finding that the cross-sectional temperature structure in the model is closely comparable to that observed in September 2010 by Inall et al. (2014) below around 250 m. Differences in stratification

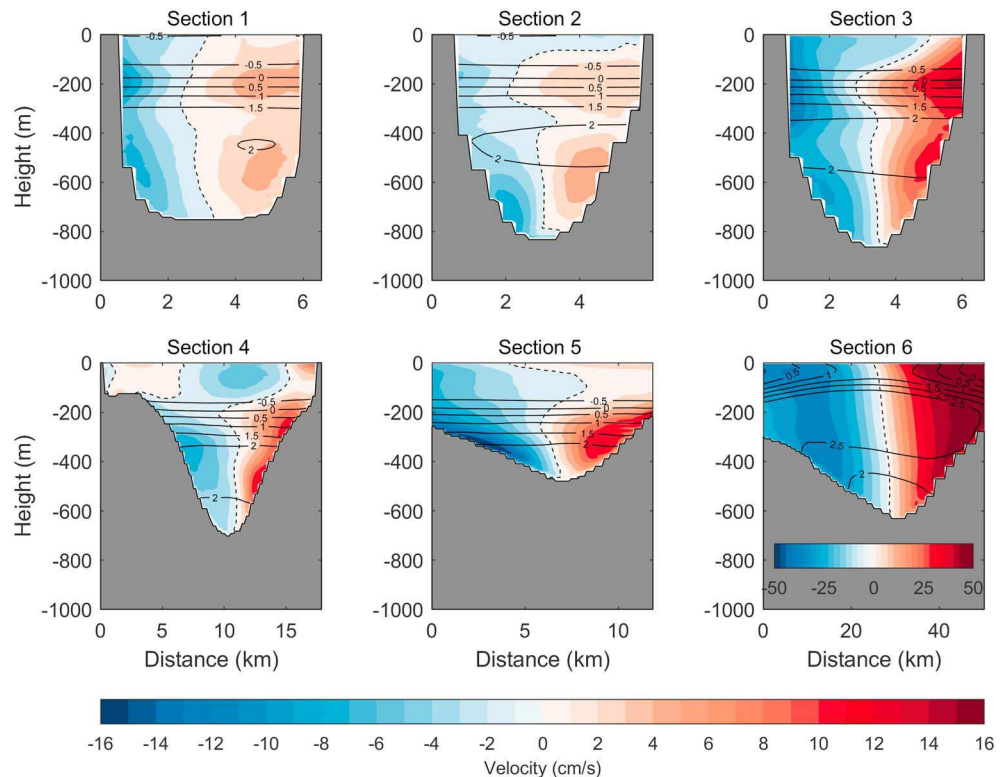


Figure 4. Mean flow normal to standard cross sections shown in Figure 2. Black contours denote conservative temperature. Note the different velocity scale for Section 6.

shallower than this depth are likely attributable to seasonal variability in freshwater runoff. Some wintertime temperature and salinity data from the shelf region of the model domain was obtained by an instrumented seal (Treasure et al., 2017) during the 4–5 January 2005. The seal performed nine dives near the southern boundary (Figure 2), sometimes exceeding 300 m depth, giving temperature measurements along its path. Figure S1 in the supporting information shows the resulting temperature field alongside the corresponding model temperature field for 4–5 January 2008, interpolated onto the seal's path. Overall, the model shows generally good agreement with the observations in terms of stratification structure, thermocline height, and the temperature in the upper and lower layers. The model does not reflect the sharp thermocline and subsurface temperature maximum seen at between 100 and 200 m depth in the observations, while the surface waters (top 50 m) are also colder in the model. This may be due to interannual variability as opposed to model inaccuracy. The close proximity to the model boundary means that this agreement may be more a validation of the boundary conditions than of the model itself.

The mean flow through six cross sections of the combined KF/KT system is shown in Figure 4, with mean isotherms overlaid. Section locations are shown in Figure 2. In KT (Section 6) we see a strongly barotropic flow regime, with inflow (outflow) of around 40 cm s^{-1} on the right (left) flank looking toward the fjord. In the fjord mouth (Sections 4 and 5) the mean flow is weaker and intensifies with depth, with current cores of around 15 cm s^{-1} concentrated against sidewalls at around 400 m depth. Moving in-fjord the currents become weaker still, while retaining the pattern of inflow on the right and outflow on the left. Isotherms reveal a strong thermocline (which coincides with the pycnocline, not shown) within KF at a mean depth of around 200 m. Absolute geostrophic velocities (not shown), calculated using the sea surface height (SSH) and density fields at each section, are in close agreement with the modeled fields, indicating that the circulation is typically in geostrophic balance to a close approximation.

We computed the overturning streamfunction from the laterally-integrated along-fjord velocity field at each cross section of the fjord interior (Figure 5), revealing any of the residual overturning circulation not obvious in the mean flow (Figure 4). At all sections, the time-mean streamfunction displays four local extrema, indicating

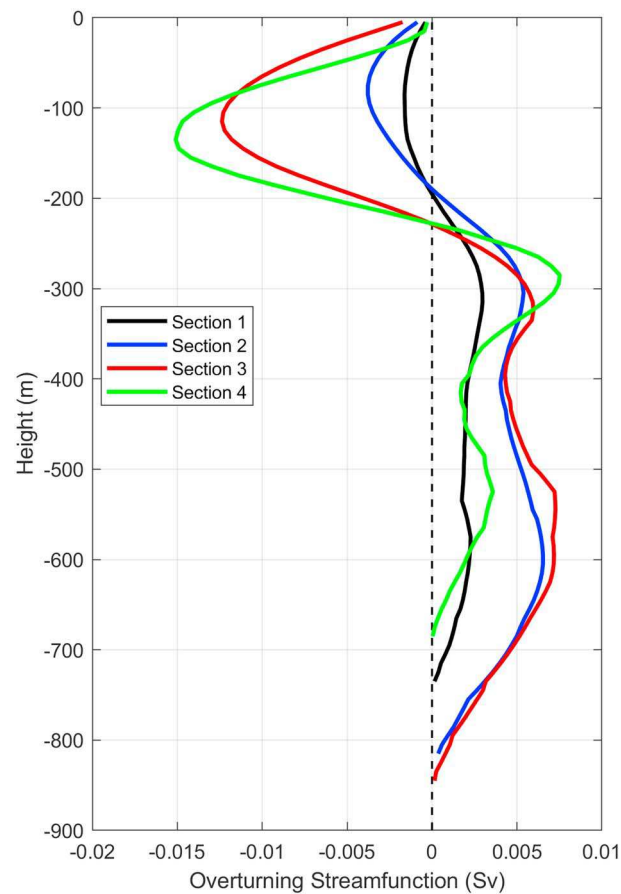


Figure 5. Mean overturning streamfunction at Sections 1–4. Positive here indicates up-fjord transport.

a complex, multi-layered circulation scheme. The strength of overturning increases moving out of the fjord, most markedly between Sections 2 and 3.

Motivated by the barotropic nature of the flow in KT, we investigated the sea surface height (SSH) anomaly on Section 6 (relative to the spatiotemporal mean), looking specifically for correspondence between wind forcing and shoreward transport. Figure 6a shows the time evolution of SSH gradients alongside the depth-averaged current (DAC) normal to the section. The surface is generally depressed in the middle of the section and elevated at either side. Barrier winds regularly correspond to a deepening of the central depression, and appear to temporarily hinder the northward DAC on the eastern side while enhancing the the southward DACs in the western side. There is a marked discontinuity between the SSH structure in the first half of December and the rest of the simulation. We suspect this is due to either the influence of the erratic wind forcing during Cluster A (Figure 3) on the Ekman layer, an artefact of the southern boundary condition changing from static to dynamic at the beginning of the simulation or both.

Figure 6b shows the density anomaly at 300 m depth, which is approximately equivalent to the height of the pycnocline. Although temporal variability is greater than lateral variability, the 1σ error bars indicate that density variability (and, hence, vertical motion of the pycnocline) is greatest toward the right-hand boundary of the fjord. The right-hand side also corresponds to the greatest variability in along-fjord velocity in the lower layer.

From density profiles within the fjord, we obtained the horizontal velocity structure associated with normal baroclinic modes of oscillation (Emery & Thomson, 1997). The linear, mode-one internal wave speed was $c_1 = 1.1\text{ m/s}$, in agreement with Inall et al. (2014). From this, we computed $L_R = c_1/f = 8.1\text{ km}$ and found the resonant seiche period to be $T = 4L/c_1 \sim 3\text{ days}$.

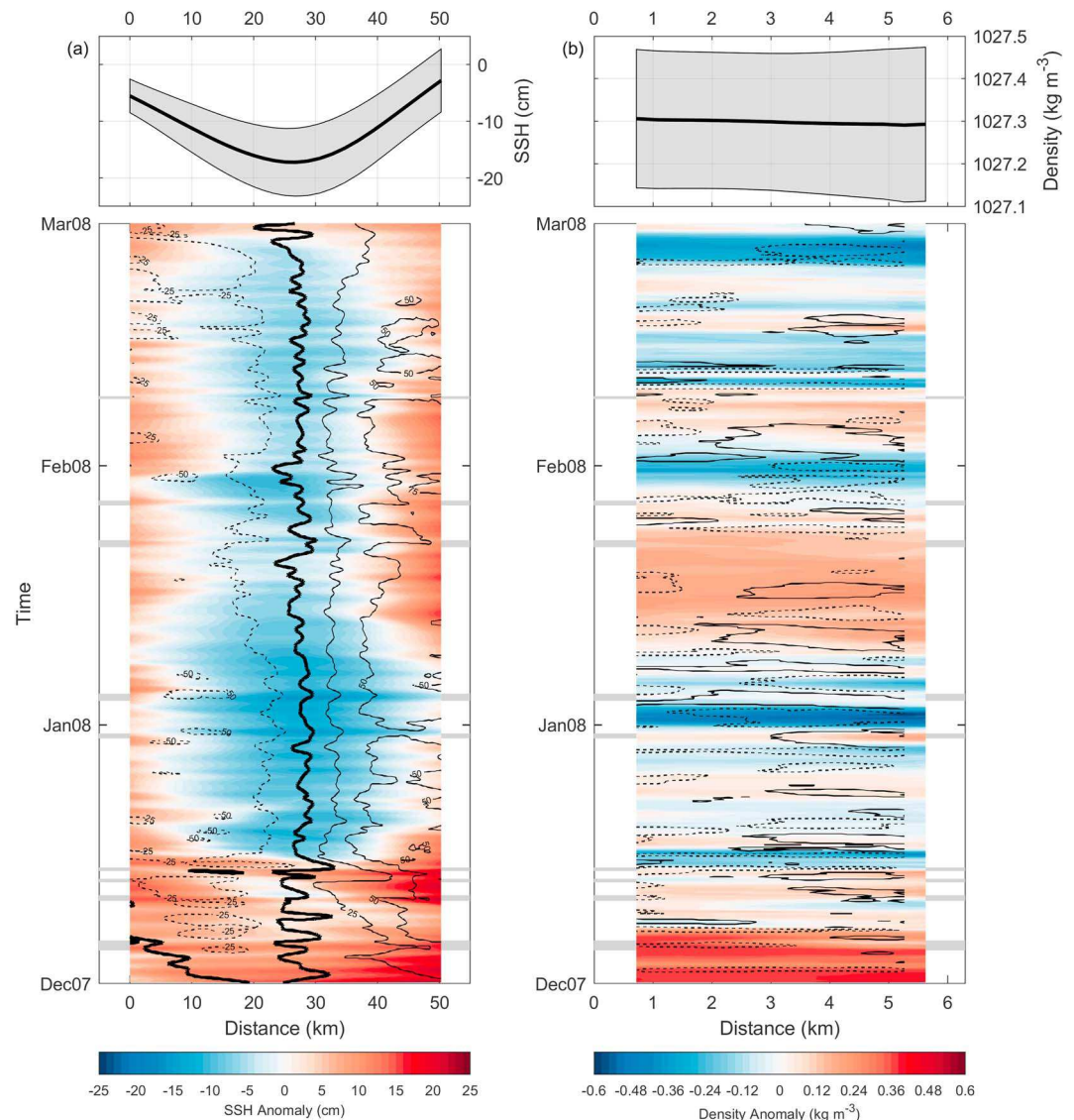


Figure 6. (a) Hovmöller diagram showing the SSH anomaly at Section 6 over the course of the simulation. Black solid (dashed) lines denote northward (southward) DAC contours (cm/s), while the black bold lines denote zero DAC. The panel at the top shows mean SSH $\pm 1\sigma$. (b) Hovmöller diagram showing the density anomaly at 300 m depth on Section 2 over the course of the simulation. Black solid (dashed) lines denote northward (southward) 10-cm/s velocity contours at 400 m depth. The panel at the top shows the corresponding mean density $\pm 1\sigma$. The bars down either side of each panel denote barrier wind activity.

We used empirical orthogonal function (EOF) analysis to isolate the statistically dominant modes of variability in the velocity field at each section of the KF interior (Sections 1–3; Emery & Thomson, 1997). Specifically, we note EOFs featuring a nodal contour corresponding to the zero-crossing in the first normal mode (around 200 m, approximately the mean pycnocline height). This pattern was seen in EOF 1 on Sections 1 and 3, accounting for 31% and 49% of the variance at their respective locations (Figure 7). On Section 2, this class of variability projected onto the second EOF which accounted for 30% of the total variance (the first EOF at Section 2, not shown, accounted for 37% of the variability and was similar in structure through more weakly sheared, with a nodal contour at around 350 m). In each of these fields, velocities above the pycnocline opposed those below, with strong vertical shear occurring at around 200 m depth. A similar vertical structure was found in the corresponding baroclinic normal modes of oscillation based on stratification (Figure S2), as in, for example, F118; Sutherland and Straneo (2012). This pattern of vertical variability is most intense adjacent to the eastern sidewall of the fjord and weakens toward the fjord interior. In Sections 2 and 3 this trend continues to the

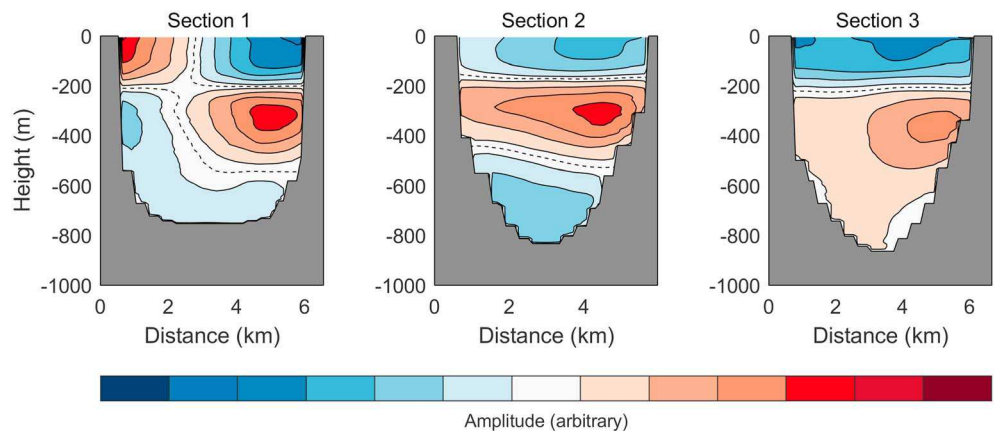


Figure 7. EOF 1 at Sections 1 and 3, and EOF 2 at Section 2, accounting for 31%, 49%, and 30% of the velocity variability at Sections 1–3, respectively. Here red opposes blue, while white represents no motion.

western side of the fjord, while in Section 1 the pattern reverses west of the fjord centerline and intensifies again toward the western sidewall. The temporal variability of the EOF coefficient at each section was seen to increase with barrier wind forcing. As this was shown by FI18 in a very similar study, it is not shown again here.

Figure 8 shows a time series of horizontal velocity, (u, v) where u is the across-fjord component and v is the along-fjord component, averaged over the Section 2 lower-layer inflow region (defined as $z < -200$ m, $\bar{v} > 3$ cm/s, Figure 4). Velocities are largely directed along-fjord, regularly alternating in sign. Cross-fjord velocities are maximal during these transitions but are smaller by an order of magnitude. The largest along-fjord velocities, along with the most frequent sign changes, generally occur in the days immediately following barrier wind event clusters on the shelf. During these times, the vectors describe a highly prolate ellipse.

Figure 9 shows a time series of the model-generated temperature profile 500m from the eastern boundary of Section 2. Quasi-periodic oscillations in the height of the thermocline persist throughout the simulation, although the shape, amplitude and frequency of the waveforms is highly variable. Furthermore, the thickness of the thermocline (defined as $-0.5 < \Theta < 1.5^\circ\text{C}$) changes during the simulation, increasing from an initial value of around 50 m to reach almost 200 m, with a subsequent decrease coincident with increasing lower-layer temperature.

Wavelet analysis was used to decompose the velocity variability in frequency space. Similar to Fourier analysis, this method has the added advantage that the amplitude at each basis frequency may vary temporally, allowing a spectral perspective on the model's response to either stochastic or externally forced variability on the shelf. We performed the analysis on the along-fjord component of the Section 2 lower layer inflow (Figure 8), using a Morlet wavelet basis function (Figure 10; the different basis options are detailed in Torrence & Compo, 1998, along with a comprehensive description of the procedure). The most significant harmonic variability occurs with period 2–4 days, consistent with the predicted resonant seiche period. There is a strong

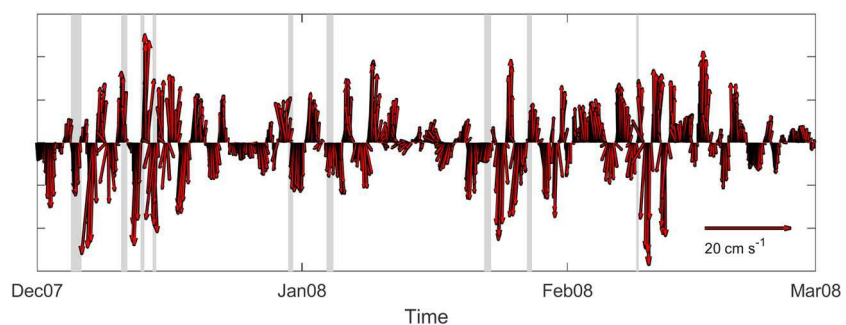


Figure 8. Horizontal velocity time series, averaged over the deep layer inflow region of Section 2. The y-axis represents along-fjord velocity (normal to section), and the x-axis shows across-fjord velocity (parallel to section). The grayed-out regions denote periods considered barrier wind events on the shelf.

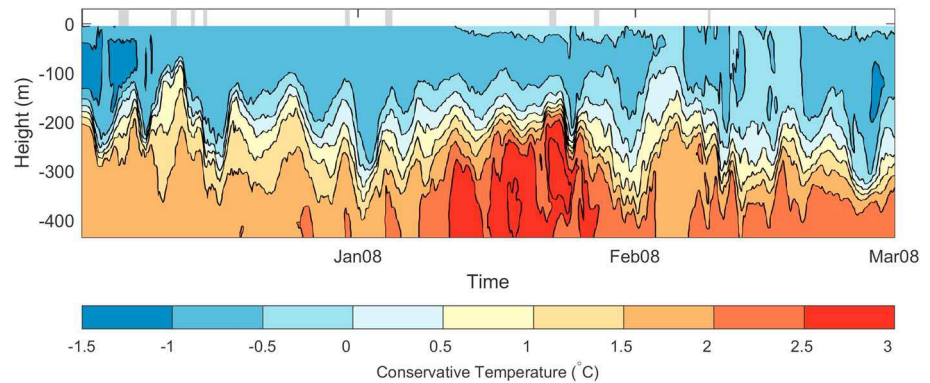


Figure 9. Temperature profile time series near the eastern end of Section 2. The gray bars at the surface denote barrier wind events on the shelf.

coincidence between barrier wind activity and excitation of this period band, with the frequency-averaged wavelet power exceeding the 95% confidence level on four occasions (Figure 10c), each corresponding to a barrier wind event cluster. Harmonic variability also occurs with period ~ 25 days, which is broadly consistent with the interval between wind event clusters. However this period lies largely within the cone of influence (Figure 10a), introducing the risk of spurious signals due to edge effects, and does not exceed the 95% confidence interval (Figure 10b).

Defining exchange as

$$Q = \frac{1}{2} \iint |v(x, z)| dx dz \quad (1)$$

where x and y are the respective across- and along-fjord coordinates, we calculated time series of the exchange through each cross section (Figure S3). In the fjord mouth (Sections 4 and 5) barrier wind events are commonly followed by spikes in exchange, particularly following the first wind event of each cluster. The exchange through KT (Section 6) appears less sensitive to variability in wind patterns over short timescales. The maximum correlation between the Sections 5 and 1 time series occurred at a lag time of 14 hr, with a correlation coefficient of 0.94. The two sections are approximately 55 km apart, indicating that information propagates

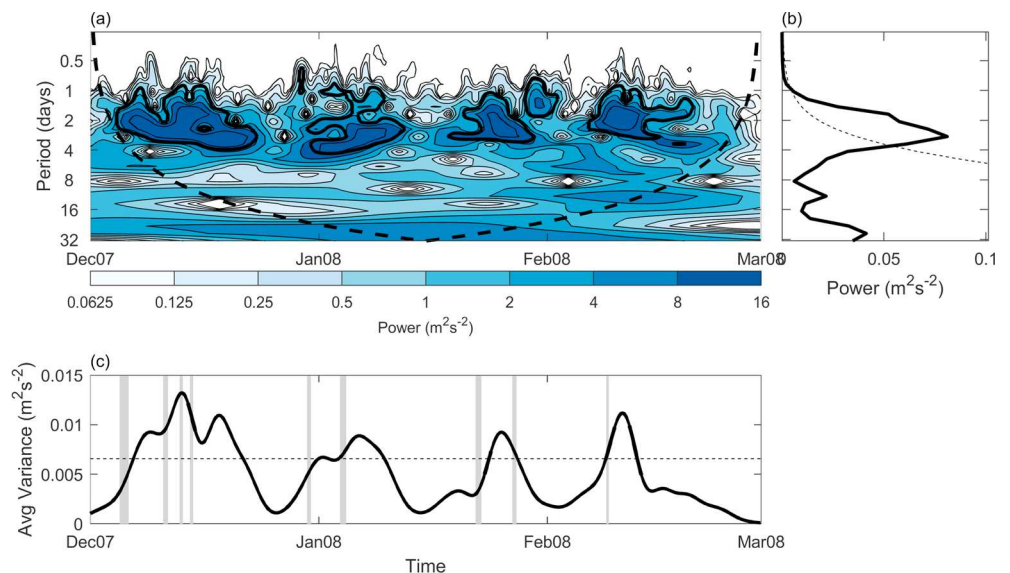


Figure 10. (a) The local wavelet power spectrum from velocity variability at the Section 2 lower layer inflow region, black thick contours enclose regions of 95% confidence or greater, while the the region below the dashed line is the cone of influence, where we expect edge effects to become important; (b) the Fourier power spectrum, where the dashed line represents the 95% confidence level; (c) frequency-averaged wavelet power, with the dashed line representing the 95% confidence level. The grayed-out regions denote periods considered barrier wind events on the shelf.

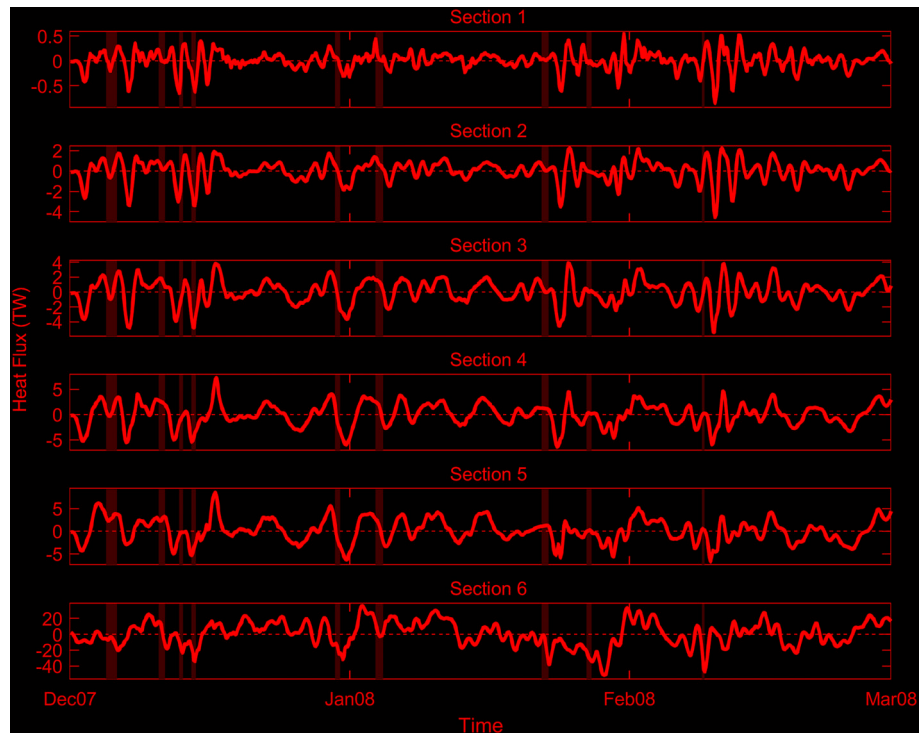


Figure 11. Heat flux through each of the standard cross sections of the KF/KT system. Note the different ordinate scales. The grayed-out regions denote periods considered barrier wind events on the shelf.

up-fjord at around 1.1 m/s, the predicted mode-one internal wave speed. This result holds for any chosen pair of fjord cross sections, though it is best seen when the sections are further apart.

Defining advective heat flux as

$$Q_{\Theta} = C_p \rho_0 \iint v(x, z) \Theta(x, z) dx dz \quad (2)$$

where C_p is the specific heat capacity of seawater and ρ_0 is reference density, we calculated time series of the heat flux through each cross section, shown in Figure 11. The mean, standard deviation, and maximum heat flux values through each section are shown in Table 1. Barrier wind activity generally results in an oscillating heat flux signal at all locations, and hence the standard deviation is two orders of magnitude larger than the mean at each section. The amplitude of the oscillation decreases by around a factor of 10 between the fjord mouth and the fjord head. The response to each wind event is inconsistent, differing in amplitude, frequency and number of cycles. For example, the response to Cluster B is manifest as a relatively low-frequency oscillation, compared to the responses to Clusters A, C, and D. Furthermore, there is evidence of coherent signal propagation which is not obviously caused by barrier wind forcing. Figure 12 shows the cumulative time-integral of the heat flux plots shown in Figure 11. The maximum correlations, with coefficient 0.27, between the heat flux time series at Sections 5 and 1 suggest a signal propagation speed of around 1.5 m/s,

Table 1
Mean, Standard Deviation, and Maximum Heat Flux (TW) Toward KG Through Each Section

| Section no. | Mean | σ | Max. |
|-------------|-------|----------|-------|
| 1 | 0.003 | 0.185 | 0.540 |
| 2 | 0.012 | 1.022 | 2.275 |
| 3 | 0.014 | 1.608 | 3.894 |
| 4 | 0.019 | 2.254 | 7.294 |
| 5 | 0.171 | 2.567 | 8.580 |
| 6 | 0.572 | 15.61 | 36.00 |

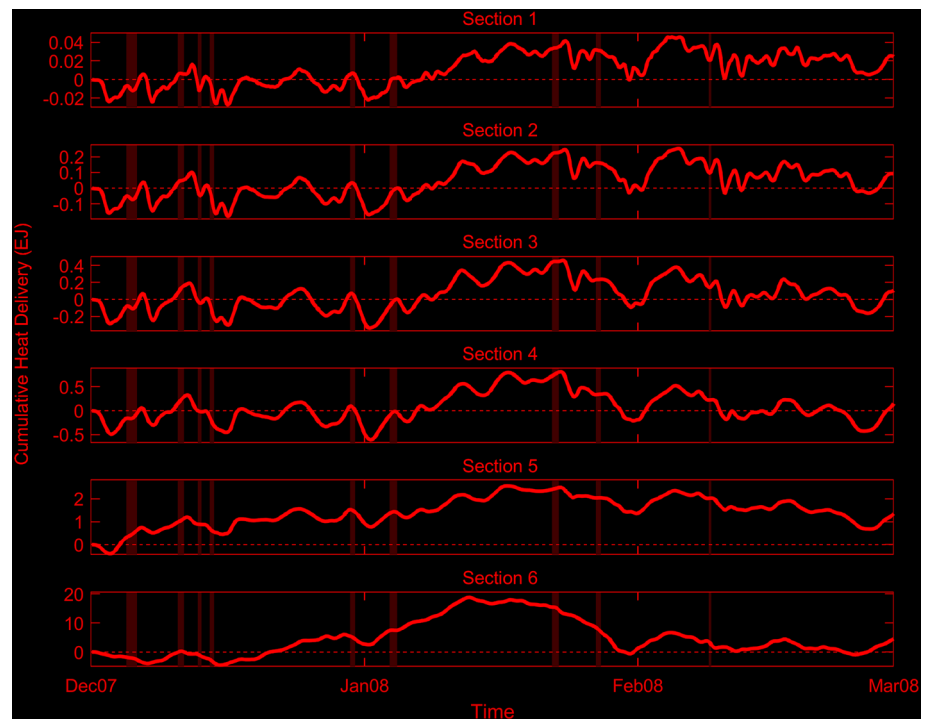


Figure 12. Time integral of the heat delivered through each of the standard cross sections of the KF/KT system. Note the different ordinate scales. The grayed-out regions denote periods considered barrier wind events on the shelf.

suggesting that the heat flux signal propagates faster than the exchange signal. This may be a result of the heat flux signal being driven by both intermediary circulation (propagating at 1.1 m/s) and additional advection by the cyclonic background flow (Figure 4).

We calculated the internal wave energy flux, $\overline{v'P'}$, through each cross section, where v' and P' are the time-varying deviations from the mean along-fjord velocity and mean pressure respectively (Nash et al., 2005). Figure 13 shows the time-mean energy flux through each section. There is a net energy flux into the fjord through all sections, concentrated on the right-hand side of the fjord at around 300 m depth. Incoming wave energy therefore corresponds to both up-fjord mean flow (Figure 4) and flow variability (Figure 7). It is evident that the incoming wave is relatively nondispersive, with a maximum of around 20 W/m² throughout the fjord (Sections 1–4). The significant down-fjord wave energy flux on the left-hand side of Section 1 indicates that waves can propagate around the fjord head efficiently. However, the outgoing wave energy flux decays quickly moving out fjord, and by the fjord mouth (Section 4) is significantly smaller than the incoming flux. The time-mean energy flux through the fjord mouth (Section 4) was 2.7 MW (directed into the fjord).

Subgrid-scale mixing parameters were calculated on the 300 m depth level, as this depth corresponds to a local maximum in both vertical and horizontal diffusivity which is not related to the surface or bottom boundary layers (Figure 14). The KPP-generated vertical diffusivity, κ_z , was greatest near the right-hand boundary near the fjord mouth and increased from a background value of around 3×10^{-4} m²/s in the fjord interior to around 8×10^{-4} m²/s following barrier wind events. Horizontal diffusivity, κ_h , which we recovered from the model-generated biharmonic viscosity according to Fox-Kemper and Menemenlis (2008), equation (33), was more uniformly distributed in both space and time, although values were again higher near fjord sidewalls where the mean values were around 2 m²/s.

We investigated the role of shear dispersion a process whereby an effective horizontal diffusivity, κ_{sd} , is induced by vertical mixing in a vertically sheared flow. Young et al. (1982) estimate that in an oscillating flow,

$$\kappa_{sd} = \frac{1}{2} \left(\frac{\alpha}{\omega} \right)^2 \kappa_z \quad (3)$$

where α is the maximal velocity shear and ω is the angular frequency of oscillation. From this expression, we found that the mean horizontal diffusivity increased by 0.6 m²/s due to shear dispersion at 300 m depth,

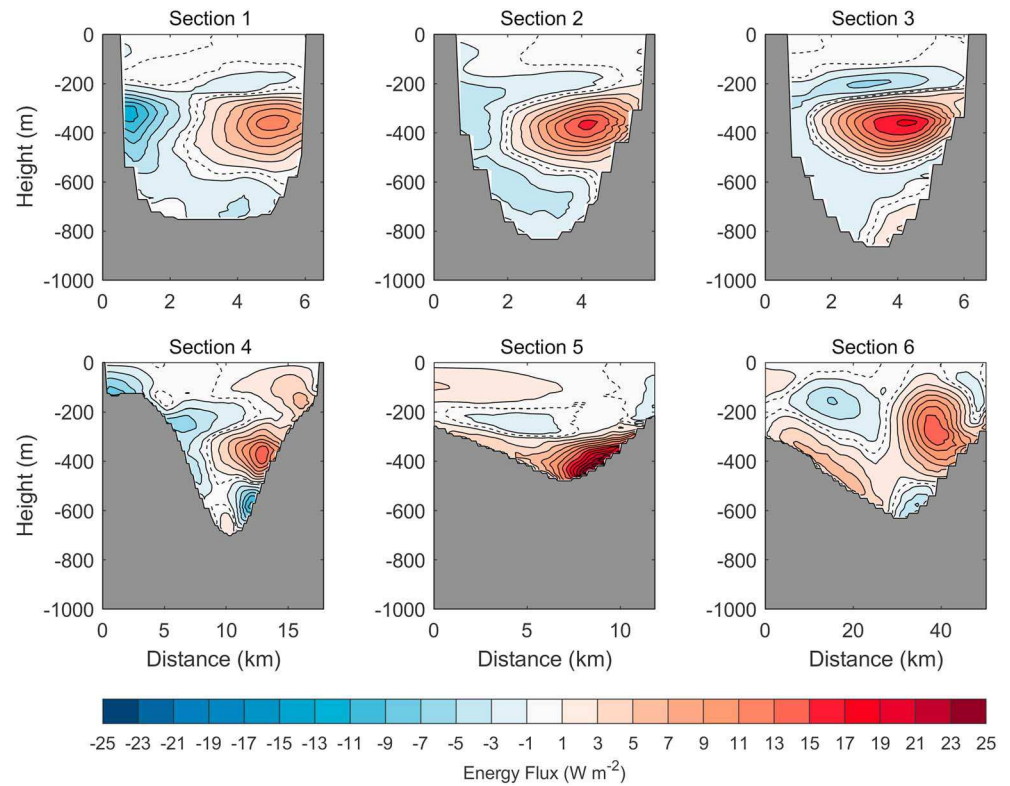


Figure 13. Time-averaged wave energy flux through each cross section, with positive values indicating energy flux into the fjord and a dashed line denoting the zero contour.

effectively doubling the mean value. Spatial patterns in shear dispersion are inherited directly from those in κ_z , resulting in a much greater contribution toward horizontal diffusivity at the right-hand boundary where values reached $100 \text{ m}^2/\text{s}$.

Figure 15a shows the time-mean melt pattern on the ice face at the northern boundary of KF. Melting is small in the upper layer and increases with depth, peaking at 350 m where the time-mean melt rate is 0.21 m/day . Melting is also weaker at the lateral boundaries of the ice face so that strong melting is concentrated in the middle of the ice face, where the melt rate reaches a maximum of 1.0 m/day . This is likely due to the dependence on flow speed in the adjacent cells (Cowton et al., 2015). We generated a time series of face-averaged melting over the course of the simulation (Figure 15b). Variability in melting occurs on timescales of 2–4 days, corresponding to the dominant period of the internal wave field. We find a correlation coefficient of $r = 0.86$ between time series in face-averaged melt rate and adjacent flow speed, while $r = 0.30$ between melt rate and adjacent temperature. Although parametrized melt rate is explicitly dependent on the both the temperature and the velocity adjacent to the ice face (Jenkins, 2011), the range of temperatures in direct contact with the ice is relatively small. Instead, the large changes in flow speed at the head of the fjord make this the dominant control over melting in the model.

The melt rates were spatially integrated to find the total volume melted per unit time, dV/dt , which was then converted into an effective heat delivery from the ocean to the ice sheet using

$$Q_i = \frac{dV}{dt} \rho_i (C_i \Delta\Theta + L_i) \quad (4)$$

where $\rho_i = 930 \text{ kg/m}^3$ is the density of ice, $C_i = 2,100 \text{ J kg}^{-1} \text{ K}^{-1}$ is the specific heat capacity of ice, $\Delta\Theta = 10 \text{ K}$ is the temperature below freezing point of the glacier, and $L_i = 334,500 \text{ J/kg}$ is the latent heat of melting ice. We obtain $\overline{Q_i} = 1.7 \text{ GW}$ and $Q_i^{\text{max}} = 4.6 \text{ GW}$, indicating that over half of the net northward heat supply through Section 1 (Table 1) goes toward melting ice. That the maximum value is two orders of magnitude smaller than the maximum advective heat flux through Section 1 highlights the large temporal variability in Q_Θ .

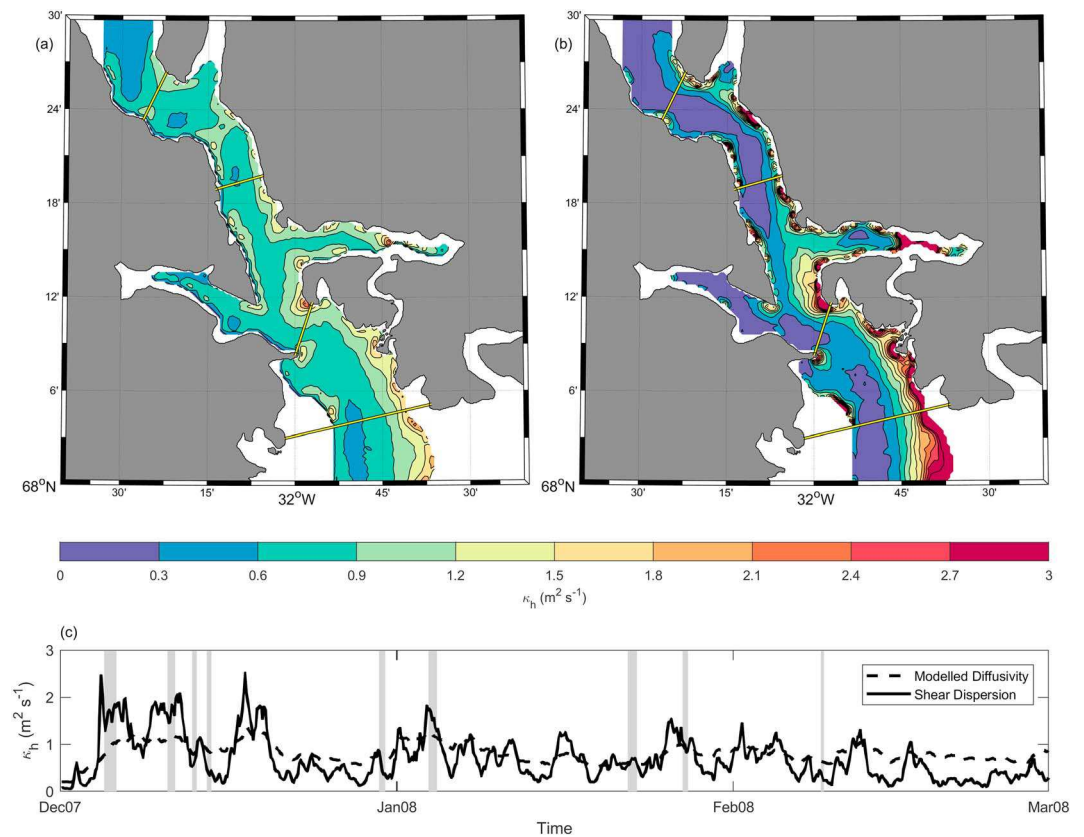


Figure 14. Mean subgrid-scale horizontal diffusivity at 300 m depth (a) from model generated fields and (b) from shear dispersion (vertical diffusivity can be recovered approximately by dividing the shear dispersion values by 2,500). (c) Corresponding time series of the spatially averaged values. The grayed-out regions denote periods considered barrier wind events on the shelf.

4. Discussion

4.1. Cross-shelf Transport

The SSH and velocity fields on Section 6 show the mean flow to be largely barotropic due to the lack of apparent vertical velocity shear (Figure 4), with cyclonic circulation ($>50\text{cm/s}$) supplying shelf waters to the fjord mouth (Movie S1). Although the variability in along-KT transport appears relatively unaffected by wind activity, barrier wind events generally coincide with local maxima in exchange, Q (Figure S3, Section 6), and local minima in heat flux, Q_0 (Figure 11, Section 6). We interpret this as a first-order response to the offshore barotropic pressure gradient caused by shoreward Ekman transport. The resulting offshore current superposes with the cyclonic pattern in KT, temporarily weakening the inflow on the eastern side of KT while strengthening the outflow (Figure 6). This provokes a decrease in northward net heat transport in KT (Figure 12, Section 6).

Following Cluster B, the shoreward heat flux through Section 6 remains positive throughout the first half of January (Figure 11). This period also corresponds to a small but sustained increase in cross-shelf exchange at Section 6 (Figure S3). The two wind events in Cluster B are maxima of long periods of generally increased wind speed and are hence different in character to most other barrier wind events during the simulation, which were typically stronger, shorter gusts with a lifespan of around 2 days. For example, the second wind event in Cluster B occurred during the longest uninterrupted spell of northeasterly wind speeds in excess of 10m/s during the record, which lasted 3.75 days. The wind events during Cluster B were also weaker than many others during the simulation (Figures 3a and 3b), barely meeting the criteria of 20m/s set by Harden et al. (2011). We investigated this further by decomposing the variability of the 10 m northeasterly wind component (Figure 3a) into frequency space, once again using wavelet analysis, which confirmed that Cluster B coincided with the most significant low-frequency variability during the record (late December/early January, Figure S4).

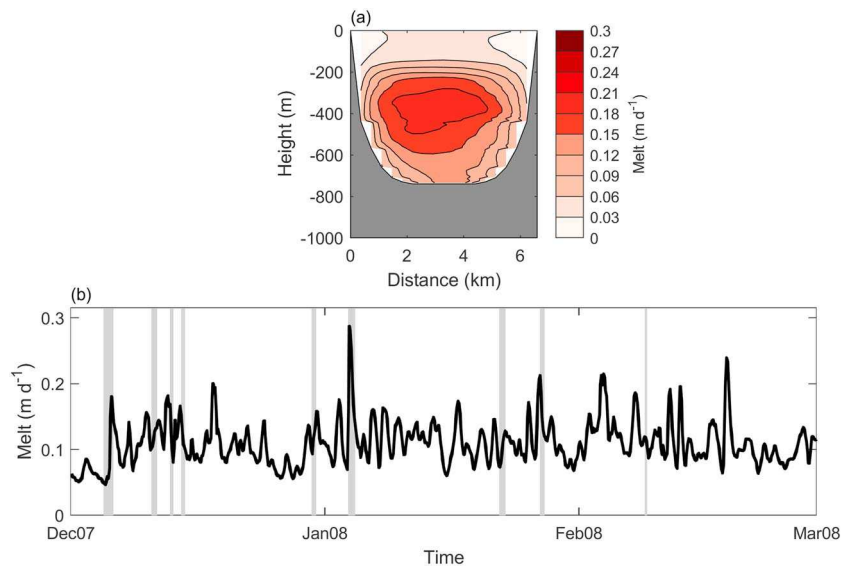


Figure 15. (a) Time-averaged melt rate simulated at the glacier terminus during DJF 2007–2008. (b) Time series of spatially averaged melting. The grayed-out regions denote periods considered barrier wind events on the shelf.

Nilsen et al. (2016) describe a mechanism whereby along-shelf winds (with coast to the right) strengthen the cyclonic circulation within cross-shelf troughs and force the currents to follow shallower isobaths in order to conserve potential vorticity. This relies upon quasi-geostrophic theory and hence holds when the wind forcing is steady, or varies on subinertial timescales. Assuming that the KT system behaves similarly, such a mechanism would explain the period of sustained positive heat flux through KT in the first half of January, when along-shelf winds were sustained and exhibited low-frequency variability. With temperatures in northern KT and the fjord mouth region increased, subsequent fjord-shelf exchange would have led to warming of the KT interior, as seen throughout January in Figures 9 and 12.

We therefore assert that, based on the model presented here, the response of the shelf circulation to wind forcing may be partitioned into two contrasting regimes: Short (≤ 1 day), strong gusts of along-shore wind act to disrupt cross-shelf transport in KT by altering the barotropic pressure gradient on inertial or superinertial timescales, while, conversely, lower-frequency (or sustained) wind forcing provides sufficient time for the cyclonic circulation to adjust to the increased barotropic pressure gradient. In the second case, the enhanced barotropic circulation in KT acts to increase cross-shelf delivery of AW. This dependence of the heat supply to the fjord mouth on the behaviour of the wind field is not captured in previous modeling studies of wind-driven fjord-shelf exchange (Cowton et al., 2016; Sciascia et al., 2014), highlighting the advantages of the combined fjord-shelf domain employed here. Without this approach, the largest heat delivery events (following Cluster B, Figure 12) would not have been captured.

4.2. Circulation in the Fjord Interior

In accordance with intermediary circulation as outlined by Straneo et al. (2010) for SF, barrier winds initially produced a negative heat flux in the fjord interior due to upper-layer inflow, which model animations reveal to be a redirected branch of the EGCC (Movie S2). This is followed by a positive contribution from lower-layer inflow (Movie S2 and Figure 11), and the expelled water in the upper layer rejoins the cold, coastal current.

The EOF patterns in Figure 7 are symptomatic of CTW activity, due to the intensification of flow variability toward the eastern side. We hence suggest that information about on-shelf wind variability propagates into the fjord interior in the internal wave field via subinertial CTWs. Movie S1 and Figure 16 give a qualitative description of the CTW structure, as vertical displacements in the $S_A = 34$ g/kg isohaline surface (representative of the pycnocline) can be seen propagating from the shelf into the fjord along the right-hand boundary of the fjord mouth. Based on the model presented here, CTWs are the dominant mechanism for exchange in KF during the winter.

Inall et al. (2015) observed subinertial CTW behaviour in Kongsfjorden, a broad fjord in Svalbard, similarly forced by nonlocal wind activity. Carroll et al. (2017) see inertial Kelvin waves (i.e., CTWs at a vertical wall)

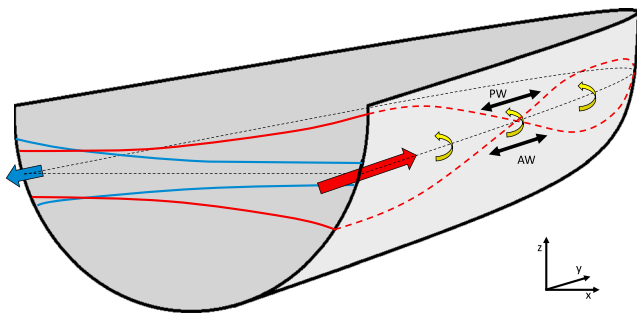


Figure 16. Schematic showing CTW activity in an idealized, Northern Hemisphere fjord where $L_R/W \approx 1$. The neutral pycnocline height is indicated in dashed black. The red (blue) arrow indicates the propagation of incoming (outgoing) wave energy and is located at the wave amplitude maximum. Red (blue) solid lines indicate the cross-sectional incoming (outgoing) wave envelope. Notice that wave energy decay effectively moves the interference zone (where the red and blue lines intersect) to the left of the fjord centerline. The red dashed lines show the longitudinal structure of the incoming wave at the right-hand boundary, with black arrows denoting the associated velocities in the PW and AW layers. Note that these velocities oppose each other and reverse over the course of a wave cycle. The yellow arrows represent shear-driven diapycnal mixing and associated strengthening of the overturning circulation.

arise via tide-sill interactions in idealized broad fjord models under summer conditions, without intermediary forcing. Similarly, Støylen and Weber (2010) see tidal generated CTWs emerge in a simulation of Van Mijenfjorden, Svalbard. This activity is hence not exclusive to SE Greenland and is seemingly the natural response, in broad fjords, to a variety of stimuli. CTWs are not captured in two-dimensional simulations of fjord-shelf exchange (Sciascia et al., 2014) or using horizontally uniform boundary forcing at the fjord mouth (Cowton et al., 2016), again illustrating that exchange between fjord and shelf is best understood when the two regions are considered in a single framework (as is also done in F118 and Jackson et al., 2018).

The model-generated mean advective heat flux values (Table 1) were generally consistent with F118, further constraining estimates of the oceanic contribution to melting at KG during the winter months. While these values appear small in comparison to those of Cowton et al. (2016), who saw summer monthly mean values exceed 1 TW in KF, this is not a true comparison as Cowton et al. (2016) considered only the up-fjord heat flux as opposed to the net. The maximal values of 2.2 TW in the mid-fjord (Section 2) and 0.5 TW at the fjord head (Section 1) are in excess of observed values, which were taken in summer. Inall et al. (2014) reports 0.26 TW through an equivalent Section 2, while Sutherland, Straneo, et al. (2014) report 0.003 and 0.19 TW through equivalent Sections 1 and 2, respectively. The high

temporal variability, associated with CTW activity, highlights the danger in taking synoptic sections of broad fjords as representative of the mean flow. The strong resemblance between Figure 6 of Inall et al. (2014) and the EOFs shown in Figure 7 leads author MEI to re-emphasize that although in geostrophic balance, the reported heat transport value of 0.26 TW from Inall et al. (2014) should be interpreted as a synoptic value, that may alias some subinertial variability around an unknown mean. This consistency between modeling and observational results further validates the model, and also indicates that CTWs influence the KF circulation in summer. It is not clear how sensitive these heat flux values are to the choice subgrid-scale mixing regime, which influences nature of the flow field.

The broadly similar temporal patterns in the heat flux time series at each section (Figure 11) indicate coherent communication between fjord and shelf. Although changes in shelf temperature are quickly manifest in the fjord mouth and interior, the lag times between sections suggest that information of lower layer inflow/outflow propagates up-fjord in the internal wave field as opposed to anomalous warm or cold patches advecting from KT to the head of KF. The (time-mean) temperature field shows an along-fjord temperature gradient in the lower layer (Figure 4), resulting in a reduced vertical temperature gradient toward the fjord head. This is consistent with the order-of-magnitude decrease in the scale of heat flux variability between the fjord mouth (Sections 4 and 5) and the head of the fjord (Section 1). The decay in the heat-flux signal is hence greater than the decay in wave-energy moving up-fjord (Figure 13). In the mid-fjord, along-fjord advection mediated by the internal wave field is associated with high-frequency variability in the heat content of the water column throughout the simulation (Figure 9). However, it is following the low-frequency Cluster B wind events, when an abundance of AW was present in northern KT, that lower-layer temperatures are seen to increase most significantly and enduringly (Figure 9).

The Burger Number, Bu , captures the relative importance of stratification to potential vorticity over sloping topography:

$$Bu = \left(\frac{NH}{fL} \right)^2, \quad (5)$$

where N is the buoyancy frequency, f is the Coriolis parameter and H/L is the topographic slope. The very high time-mean values of $Bu \sim 400$ in the mid-fjord indicate that the steep topography and strong stratification dominate over rotational effects. By comparison, we obtained $Bu \sim 0.8$ in KT, indicating that the weaker stratification and shallower slope may introduce greater nonlinearity permitting rapid dispersion. Hence, we observe a less distinct wave-like response in Section 6 of Figure 11.

It is illuminating to approximate these CTWs as Kelvin waves in a two-layer system (FI18; Jackson et al., 2018; Støylen & Weber, 2010; Inall et al., 2015). The vertical pycnocline displacement, ξ , and the depth-integrated upper- and lower-layer velocities, (U_1, V_1) and (U_2, V_2) , of such a wave can be modeled analytically (Jackson et al., 2018; Støylen & Weber, 2010) as

$$\xi(x, y, t) = Ae^{x/L_R - \beta y} e^{i(ky - \omega t)} \quad (6)$$

$$U_1(x, y, t) = -U_2(x, y, t) = 0 \quad (7)$$

$$V_1(x, y, t) = -V_2(x, y, t) = Ac_1 e^{x/L_R - \beta y} e^{i(ky - \omega t)} \quad (8)$$

where the Cartesian basis orientation is as depicted in Figure 16 and $x = 0$ is the right-hand boundary. Here A is the wave amplitude, k is the wave number, ω is the angular frequency and β is a longitudinal damping coefficient. Approximating $U_1 = U_2 = 0$ appears justified, to first order, based on the small cross-fjord velocities in Figure 8. In this simple, linear model, CTWs are nondispersive and hence propagate at the speed of a mode-1 internal wave, consistent with the good agreement between the theoretical and observed wave speed of $c_1 = \omega/k = 1.1$ cm/s. Based on the significant response of the $\omega \sim 3$ rad/day (Figure 10), we estimate $k \sim 0.02$ rad/km. This corresponds to a wavelength, $\lambda = 4L \sim 240$ km, with $L \sim 70$ km in our model. While this simple linear model does not capture (nonlinear) amplitude dispersion, wave energy dissipation is described by the parameter β . We observed wave amplitudes decay from $A \sim 70$ m at the fjord entrance (Section 4) to $A \sim 50$ m at the fjord head (Section 1), two locations separated by a distance of $\Delta y \sim 55$ km, resulting in an estimate of $\beta \sim 6 \times 10^{-6} \text{ m}^{-1}$.

From equations (6)–(8), CTW amplitude decays laterally on an e -folding length-scale of L_R . In our case, with $W/L_R \approx 1$, amplitudes are hence significant at the opposing fjord boundary, as is evidenced by Figure 6b. We expect the incoming wave to have an amplitude of A/e at the left hand boundary (~ 25 m at Section 3). Given a sufficiently strong outgoing wave signal, the incoming and outgoing waves may therefore interact, resulting in resonance (Figure 16). The opposing pattern found near the western bank of Section 1, EOF 1 (Figure 7) indicates that CTWs are either reflected or topographically steered around the head of the fjord (in the $\lambda \gg W$ regime we presume these two processes to be roughly equivalent). However, the comparatively weak outgoing wave energy signal in Sections 2–4 of Figure 13 indicated that the outgoing signal decays rapidly with increasing distance from the glacier terminus. For a fjord cross section (arbitrarily taking the section $y = 0$) where the incoming and outgoing wave amplitudes are A and B , with $A > B$, the pycnocline displacement will be a superposition of the two signals:

$$\xi(x, t) = Ae^{x/L_R} e^{-i\omega t} + Be^{-(x+W)/L_R} e^{-i\omega t} \quad (9)$$

We may have resonant motions if the condition $Be \geq A$ is met in KF, or in general if $Be^{W/L_R} \geq A$. This is demonstrated in Figure 16, where we expect a strong resonant interaction in the interference zone (where the red and blue lines intersect). Consistent with equation (9), the shaded region in Figure 6b (representing the wave envelope at Section 2) is qualitatively comparable to the superposition of the incoming and outgoing wave envelopes. Velocity variability is dominated by the predicted resonant period band at Section 2 (Figure 10), reinforcing that this interaction plays a role in determining the timescales for water mass exchange in KF. The importance of this interaction wanes moving out-fjord, as A dominates over B due to wave energy dissipation.

Hence, while FI18 argued that KF was a broad fjord, evaluation of L_R here suggests KF may be classified as an intermediate case between broad and narrow fjords and hence displays both broad- and narrow-fjord behaviour. The horizontally sheared mean flow through all cross-fjord sections reaffirms the assertion, made by FI18, that rotational effects are important, as expected in a broad fjord. Horizontal shear apparent in the snapshots of cross-sectional flow by Cowton et al. (2016) further indicate that the KF flow field will tend toward three-dimensionality, even when conditions at the fjord mouth are laterally uniform. At the same time, the strong response around the resonant frequency would not be anticipated in the $W/L_R \gg 1$ regime, where the incoming and outgoing waves are spatially distinct and hence cannot interfere significantly. This result is consistent with the theoretical predictions of (Jackson et al., 2018), who find that rotational effects are of order one importance when $W/L_R > 0.5$.

While equations (6)–(8) appear to capture the wave mechanics to leading order, divergences from this approximation are evident in our numerical model output due to nonlinear effects and nonidealized stratification.

While v dominates over u in Figure 8, the assumption that u vanishes everywhere is clearly violated. The more sophisticated nonlinear two-layer approach of Støylen and Weber (2010) is required to model these motions analytically, and although we do not follow this formulation here, we exploit some of the resulting outcomes. For example, the nonlinear approach of Støylen and Weber (2010) yields a depth-averaged expression for Stokes' drift (Stokes, 1847), v_S , given by

$$v_S(x, y) = \frac{c_1 A^2}{2H_1^2} e^{2(x/L_R - \beta y)} \quad (10)$$

where H_1 is the thickness of the upper layer. Evaluation of equation (10) based on the parameters in the model yields a Stokes' drift of $v_S \sim 5$ cm/s at the fjord boundary, decaying rapidly (with an e -folding length-scale of $L_R/2$) moving toward the opposite side. This is consistent with the horizontal structure seen in the model mean flow (Figure 4), while the vertical structure is consistent with the theoretical vertical structure for Stokes' drift due to internal waves (Wunsch, 1973), with velocity maxima above and below the wave energy maximum (Figure 13). Furthermore, the velocities are comparable with the theoretical prediction of $v_S \sim 5$ cm/s and, being quadratic in wave amplitude, decrease moving in-fjord. This analysis reinforces the assertion made by FI18 that Stokes' drift is a significant driver of the mean flow in KF and, by extension, other broad fjords (Inall et al., 2015; Støylen & Weber, 2010).

Støylen and Weber (2010) also show that boundary friction gives rise to significant depth-averaged Eulerian drift, v_E , given by

$$v_E(x, y) = \sqrt{\frac{\beta}{C_D H_1}} e^{(x/L_R - \beta y)} \quad (11)$$

where C_D is the frictional drag coefficient. Based on a nominal value of $C_D = 1 \times 10^{-3}$ (Nøst, 1994; Støylen & Weber, 2010) we obtain an Eulerian drift of $v_E \sim 0.5$ cm/s, an order of magnitude smaller than v_S . This contrasts the results of Støylen and Weber (2010), who found $v_E \sim 2v_S$. This is likely due to the order-of-magnitude difference in wave amplitude between this study and Støylen and Weber (2010), together with quadratic amplitude dependence of v_S . The relatively high values of v_E reported by Støylen and Weber (2010) are encountered under additional shear stress from fast ice cover, which was not present in our model but is a known feature of KF during winter. The effect may, therefore, be underrepresented.

It is evident that two-layer approximations are not fully valid based on the stratification in the model. For instance, in Section 2 of Figure 7 we see a three-layer velocity structure, which projects best onto the second normal mode (Figure S2). This is likely due to the existence of a second, deeper thermocline due to isolated water below sill depth (Figure 4). It is not clear, in this case, why Sections 1 and 3 exhibit a two-layer pattern.

4.3. Mixing in the Fjord Interior

The reversible nature of intermediary circulation (mediated here by CTWs) means that for the process to generate nonzero time-integrated heat flux requires some mixing in the fjord interior (excluding any heat lost to melting at the terminus). The temporal divergences of the isotherms in Figure 9 imply that periods vertical mixing between the PW and AW layers do occur, and are likely linked to stratified shear turbulence (Figure 14). CTWs hence drive both advection, which increases stratification, and mixing, which decreases it. These two effects appear entangled such that it is hard to link the timing of stratification changes in Figure 9 to wind forcing directly.

The cross-fjord structure of the wave energy flux (Figure 13) shows that the incoming wave dominates over the outgoing wave, indicating that intermediary circulation driven by CTWs is a nonadiabatic process where wave energy is lost to dissipation and mixing. The net wave energy flux into the fjord implies that 2.7 MW is available for mixing within the interior.

Shear dispersion was found to contribute significantly toward mixing in the model, particularly concentrated against the right-hand boundary (Figure 14b). Since $\kappa_{sd} \sim 1/\omega^2$, we expect this mechanism to be highly effective in subinertial regimes such as this. In contrast, much of the literature is concerned with near-inertial, tidal, or higher frequency regimes (Carroll et al., 2017; Støylen & Weber, 2010) which will not have such a prominent κ_{sd} component. Furthermore, the resonant value for ω will be even smaller in the reality, as KF is longer than represented in the model, indicating that shear dispersion values may exceed the values in this study.

Integrating the buoyancy flux, $\rho\kappa_z N^2$, over the fjord interior, we obtained a time-mean value of 1.25 MW. This represents the mean rate at which the potential energy of the water column increased due to water mass transformation. Given the 2.7 MW of net wave energy into the fjord, this implies a mixing efficiency of 0.46. This exceeds the typical literature value of 0.2 (Gargett, 1984) and is significantly higher than the value of 0.06 proposed for fjords by Stigebrandt (2012). This high value is a result of the KPP mixing scheme, which has previously been found to be overly diffuse in shallow or coastal regions (Durski, 2004). Nonetheless, we expect that 0.46 gives a reasonable upper bound on the efficiency of internal wave-driven water mass transformation within a SE Greenland fjord.

Integrating the diffusive vertical heat flux, $C_p \rho \kappa_z \frac{\partial \Theta}{\partial z}$, over the 300 m depth surface (at which time-mean values were maximal) gave a value of 3.7 GW. Hence, according to our model, the dissipative heat flux between the AW and PW layers is comparable to the advective heat flux toward KG (Table 1, Section 1).

The increase in the strength of out-fjord transport, moving away from the glacier front (Figure 5), implies that water mass transformation in the fjord interior is as significant as that driven by plume dynamics at the terminus. The wind-driven component of overturning is assumed to be negligible due to fast ice cover in the fjord interior. The marked increase in overturning strength between Sections 2 and 3 is therefore attributed to significant vertical density flux via diapycnal mixing. The two side fjords in this region provide additional topographic boundaries for CTWs to follow, increasing the area available for mixing at sidewalls (Figure 14), and the complex coastline drives mixing around features such as headlands. As diapycnal mixing is fed by incoming internal wave energy, this result indicates that CTWs act to increase the overturning circulation. This effect is likely exaggerated by a factor of two or more as a result of the high mixing efficiency in the model. Furthermore, an overly diffuse model would likely act to strengthen longitudinal wave decay and therefore anticipate that true value of β may be larger than that stated in the previous section.

4.4. Melting at the Glacier Terminus

Cluster B coincided with the highest melt rates in the simulation (Figure 15). The high melt rates preceded the large increase in heat content within KF (Figure 12), indicating that they are triggered by increased flow speed due to CTW propagation as opposed to increased temperature. Given the close correlation between melt rate and adjacent flow speed in the model, another potentially important factor is the capacity for CTWs to induce energetic flow in the upper reaches of the fjord. The exchange flows triggered by barrier wind forcing were in general found to decay considerably between the mid-fjord and the fjord head, while the exchange flows triggered by Cluster B remained highly significant at Section 1 (Figure S3). This effect may be greater in the real KF, which is longer than the KF represented in the model. Theory shows maximum particle speed to be linear in amplitude for long waves (Cushman-Roisin & Beckers, 2011), and we therefore attribute the strong melting to the large CTW amplitudes during Cluster B (Figure 9) as opposed to associated low-frequency Q_Θ signal which continued throughout the first half of January.

The modeled melt rates of around 0.1–0.3 m/day (Figure 15) are broadly consistent with Cowton et al. (2015) who, while introducing the iceplume package in an idealized fjord model, saw spatiotemporally averaged melt rates of 0.18 m/day in a model run without subglacial discharge. This value increased to 0.22 m/day when subglacial discharge was included, implying that the peaks in Figure 15b are comparable to summertime values. Carroll et al. (2016) found simulated summer melt rates (generated using the parametrization by Holland & Jenkins, 1999) at KG to be an order of magnitude larger than the values reported here (~ 4 m/day), although these values refer specifically to the locality of the subglacial plume rather than the spatial average over the ice front. Two-dimensional simulations of SF by Sciascia et al. (2014) saw melt rates (again from Holland & Jenkins, 1999) increase from ~ 0.2 m/day in winter to ~ 2 m/day with the addition of subglacial discharge, with the highest melt rates of all (2.2 m/day) recorded when subglacial discharge and intermediary circulation were simultaneously active. Due to the two-dimensional configuration, all melting was essentially restricted to the plume location in freshwater forced runs, which may explain the discrepancy with Cowton et al. (2015) and the (order of magnitude) agreement with Carroll et al. (2016). The two-dimensional approach permits only vertical velocities next to the ice front, making buoyant subglacial plumes the primary agent for flow-dependant melting. While this is appropriate when $W/L_R \ll 1$ (Sciascia et al., 2013, 2014; Straneo et al., 2010), the circulation described in this study suggests there is a mean (horizontal) flow across the front of the KG terminus and that, in broader fjords, large flow speeds can occur next to the ice face in the absence of freshwater forcing. Systems in this category therefore require a three-dimensional description in order to fully characterize and compare summertime and wintertime melting.

While the heat delivery to the ice sheet, Q_i , was consistent with the mean advective heat flux toward the glacier, Q_e , the modeled melt rates were two orders of magnitude smaller than the glacial flow speed at KG during 2007–2008, which was around 25m/day (Bevan et al., 2012). Our results therefore appear to suggest that ocean-driven melting during the winter was not capable of matching the rapid flow speeds observed during this period. We suspect, however, that our model underrepresents the oceanic contribution to KG frontal ablation. This is primarily a study of shelf-driven exchange, and the model lacks the sophistication to produce realistic glacier diagnostics. The iceplume package was utilized to provide a heat sink at the head of the fjord and add a level of realism to hydrography in the far field. The package is highly sensitive to the prescribed background velocity when subglacial discharge is small or zero (Cowton et al., 2015), as was the case here. Due to the static ice face geometry, the model cannot account for the triggering of calving events or instabilities in glacial flow due to ocean-driven melting at the terminus. The pattern of melting found on the ice face (Figure 15a) would in reality drive undercutting and hence encourage calving events. Furthermore, the flat ice face likely does not affect the adjacent flow realistically, as tidewater glacier termini are typically crevassed and uneven over small spatial scales. This may have caused the model to exaggerate the relative influence of adjacent flow speed over temperature.

5. Summary

A high-resolution numerical model of KF and the adjacent shelf region during winter 2007–2008 shows coherent communication between fjord and shelf, with temperature changes on the shelf able to influence the fjord interior. AW is delivered from the shelf break toward the fjord by the geostrophically balanced cyclonic circulation in KT, which is driven by sea surface tilt. The mean circulation structure in KF is similar, though weaker and with a larger baroclinic contribution, and delivers heat to the glacier terminus due to mean cross-fjord temperature gradients. Water mass transformation due to melting at the glacier front and mixing in the fjord interior adds a buoyancy-driven overturning component to the circulation, although it is the horizontal shear, which dominates the mean flow. CTWs, which are instigated by barrier winds on the shelf, emerge as the dominant mode of variability within the fjord and drive greatly enhanced along-fjord volume and heat transport. CTWs also act to enhance both the buoyancy-driven overturning circulation, via diapycnal mixing, and the cyclonic background flow, via Stokes' drift. The mechanism has previously been observed in a broad, glaciated fjord in Svalbard (Inall et al., 2015) and is likely to play a significant role in broad fjords in general.

SE Greenland coastal waters have warmed in recent years, and we have demonstrated here that barrier wind-driven CTWs have likely played a crucial role in communicating this ocean warming to the GrIS. The efficacy of CTWs in delivering heat toward the KG terminus, in a time-mean sense, is highly dependent on the temporal variability of barrier wind forcing. Typically barrier wind events are short and strong, ramping up quickly and exceeding the 20-m/s threshold for only ~6 hr. However, this class of wind forcing was not found to significantly increase fjord heat content. Rather, long-duration northeasterly wind forcing was found to strengthen the barotropic circulation in KT, increasing AW transport toward the fjord mouth, while provoking low-frequency CTWs, which are highly effective at drawing these waters up-fjord. This result points to barrier wind duration, as opposed to strength, as the controlling parameter on the wintertime heat delivery toward the GrIS.

The results indicate that significant oceanic heat (~0.5 TW) is regularly delivered from the shelf to glacier terminus during winter. The CTW exchange process is driven purely by shelf exchange and, although there may be some freshwater runoff in the winter months, this is not a necessary condition for this magnitude of heat exchange. We have encountered strong evidence that the processes occurs in the nonwinter months, though it is likely weaker and may be obscured or augmented by increased freshwater-driven overturning. Further research is required to fully understand the interaction between these two circulation schemes.

While the model was able to provide diagnostics for melt rate at the KG terminus, yielding a mean melt rate of 0.21m/day at the center of the ice face, the simplified parameterization was unable to describe the glacial impacts of ice-ocean interaction in detail. Coupled ice-ocean models, capturing glacier dynamics, calving, ice face texture, and marine icebergs, are needed to significantly further our understanding of the rapid acceleration and retreat of Greenland's tidewater glaciers.

Acknowledgments

Completion of this paper was supported by NERC grants N0406 (N. J. F.), FASTNet NE/1030224/1 (M. E. I.), and 02336 MASSMO (S. C. J.); by RITMARE (M. G. M.); and by NSF grants OCE-143348 and OCE-1129895 (T. W. N. H.). We would like to thank the team at ARCHER for the use of their facility and their support. The model output data described in this paper may be obtained at <https://erddap.sams.ac.uk/erddap/files>.

References

- Bevan, S. L., Luckman, A. J., & Murray, T. (2012). Glacier dynamics over the last quarter of a century at Helheim, Kangerdlugssuaq and 14 other major Greenland outlet glaciers. *Cryosphere*, 6(5), 923–937. <https://doi.org/10.5194/tc-6-923-2012>
- Carroll, D., Sutherland, D. A., Hudson, B., Moon, T., Catania, G. A., Shroyer, E. L., et al. (2016). The impact of glacier geometry on meltwater plume structure and submarine melt in Greenland fjords. *Geophysical Research Letters*, 43, 9739–9748. <https://doi.org/10.1002/2016GL070170>
- Carroll, D., Sutherland, D. A., Shroyer, E. L., Nash, J. D., Catania, G. A., & Stearns, L. A. (2017). Subglacial discharge-driven renewal of tidewater glacier fjords. *Journal of Geophysical Research: Oceans*, 122, 6611–6629. <https://doi.org/10.1002/2017JC012962>
- Cowton, T., Slater, D., Sole, A., Goldberg, D., & Nienow, P. (2015). Modeling the impact of glacial runoff on fjord circulation and submarine melt rate using a new subgrid-scale parameterization for glacial plumes. *Journal of Geophysical Research: Oceans*, 120, 796–812. <https://doi.org/10.1002/2014JC010324>
- Cowton, T., Sole, A., Nienow, P., Slater, D., Wilton, D., & Hanna, E. (2016). Controls on the transport of oceanic heat to Kangerdlugssuaq Glacier, East Greenland. *Journal of Glaciology*, 62(236), 1167–1180. <https://doi.org/10.1017/jog.2016.117>
- Cushman-Roisin, B., & Beckers, J. M. (2011). Internal waves. *International Geophysics*, 101, 395–424. <https://doi.org/10.1016/B978-0-12-088759-0.00013-4>
- Dee, D. P., Uppala, S. M., Simmons, A. J., Berrisford, P., Poli, P., Kobayashi, S., et al. (2011). The ERA-Interim reanalysis: Configuration and performance of the data assimilation system. *Quarterly Journal of the Royal Meteorological Society*, 137(656), 553–597. <https://doi.org/10.1002/qj.828>
- Dowdeswell, J. A. (2004). Cruise Report - JR106b. RRS James Clark Ross NERC Autosub Under Ice thematic programme, Kangerdlugssuaq Fjord and Shelf, east Greenland, (September).
- Durski, S. M. (2004). Vertical mixing schemes in the coastal ocean: Comparison of the level 2.5 Mellor-Yamada scheme with an enhanced version of the K profile parameterization. *Journal of Geophysical Research*, 109, C01015. <https://doi.org/10.1029/2002JC001702>
- Emery, W. J., & Thomson, R. E. (1997). *Data Analysis Methods in Physical Oceanography*. Elsevier.
- Fox-Kemper, B., & Menemenlis, D. (2008). Can large eddy simulation techniques improve mesoscale rich ocean models? *Ocean Modeling in an Eddy Regime*, 177, 319–337. <https://doi.org/10.1029/177GM19>
- Fraser, N. J., & Inall, M. E. (2018). Influence of barrier wind forcing on heat delivery toward the Greenland Ice Sheet. <https://doi.org/10.1002/2017JC013464>
- Gargett, A. E. (1984). Vertical eddy diffusivity in the ocean interior. *Journal of Marine Research*, 42(2), 359–393. <https://doi.org/10.1357/002224084788502756>
- Gelderloos, R., Haine, T. W. N., Koszalka, I. M., & Magaldi, M. G. (2017). Seasonal variability in warm-water inflow toward Kangerdlugssuaq fjord. *Journal of Physical Oceanography*, 47(7), 1685–1699. <https://doi.org/10.1175/JPO-D-16-0202.1>
- Harden, B. E., Renfrew, I. A., & Petersen, G. N. (2011). A climatology of wintertime barrier winds off southeast Greenland. *Journal of Climate*, 24(17), 4701–4717. <https://doi.org/10.1175/2011JCLI4113.1>
- Holland, D. M., & Jenkins, A. (1999). Modeling thermodynamic ice-ocean interactions at the base of an ice shelf. *Journal of Physical Oceanography*, 29(8), 1787–1800. [https://doi.org/10.1175/1520-0485\(1999\)029<1787:MTIOIA>2.0.CO;2](https://doi.org/10.1175/1520-0485(1999)029<1787:MTIOIA>2.0.CO;2)
- Inall, M. E., Murray, T., Cottier, F. R., Scharrer, K., Boyd, T. J., Heywood, K. J., & Bevan, S. L. (2014). Oceanic heat delivery via Kangerdlugssuaq Fjord to the south-east Greenland ice sheet. *Journal of Geophysical Research: Oceans*, 119, 631–645. <https://doi.org/10.1002/2013JC009295>
- Inall, M. E., Nilsen, F., Cottier, F. R., & Daee, R. (2015). Shelf/fjord exchange driven by coastal-trapped waves in the Arctic. *Journal of Geophysical Research: Oceans*, 120, 8283–8303. <https://doi.org/10.1002/2015JC011277>
- Jackson, R. H., Lentz, S., & Straneo, F. (2018). The dynamics of shelf forcing in Greenlandic fjords. *Journal of Physical Oceanography*, 48, 2799–2827. <https://doi.org/10.1175/JPO-D-18-0057.1>
- Jackson, R. H., & Straneo, F. (2016). Heat, salt, and freshwater budgets for a glacial fjord in Greenland. *Journal of Physical Oceanography*, 46(9), 2735–2768. <https://doi.org/10.1175/JPO-D-15-0134.1>
- Jackson, R. H., Straneo, F., & Sutherland, D. A. (2014). Externally forced fluctuations in ocean temperature at Greenland glaciers in non-summer months. *Nature Geoscience*, 7(7), 503–508. <https://doi.org/10.1038/ngeo2186>
- Jenkins, A. (2011). Convection-driven melting near the grounding lines of ice shelves and tidewater glaciers. *Journal of Physical Oceanography*, 41(12), 2279–2294. <https://doi.org/10.1175/JPO-D-11-03.1>
- Khan, S. A., Kjeldsen, K. K., Kjær, K. H., Bevan, S. L., Luckman, A., Bjørk, A. A., et al. (2014). Glacier dynamics at Helheim and Kangerdlugssuaq glaciers, southeast Greenland, since the Little Ice Age. *Cryosphere*, 8(4), 1497–1507. <https://doi.org/10.5194/tc-8-1497-2014>
- Koszalka, I. M., Haine, T. W. N., & Magaldi, M. G. (2013). Fates and travel times of Denmark Strait overflow water in the Irminger basin. *Journal of Physical Oceanography*, 43(12), 2611–2628. <https://doi.org/10.1175/JPO-D-13-023.1>
- Large, W. G., McWilliams, J. C., & Doney, S. C. (1994). Oceanic vertical mixing: A review and a model with a nonlocal boundary layer parameterization. *Reviews of Geophysics*, 32(4), 363–403. <https://doi.org/10.1029/94RG01872>
- Large, W. G., & Pond, S. (1981). Open ocean momentum flux measurements in moderate to strong winds. *Journal of Physical Oceanography*, 11(3), 324–336. [https://doi.org/10.1175/1520-0485\(1981\)011<0324:OOMFMI>2.0.CO;2](https://doi.org/10.1175/1520-0485(1981)011<0324:OOMFMI>2.0.CO;2)
- Leith, C. E. (1996). Stochastic models of chaotic systems. *Physica D*, 98, 481–491.
- Marshall, J., Adcroft, A., Hill, C., Perelman, L., & Heisey, C. (1997). A finite-volume, incompressible Navier Stokes model for, studies of the ocean on parallel computers. *Journal of Geophysical Research*, 102(C3), 5753–5766. <https://doi.org/10.1029/96JC02775>
- Moon, T., Sutherland, D. A., Carroll, D., Felikson, D., Kehrl, L., & Straneo, F. (2017). Subsurface iceberg melt key to Greenland fjord freshwater budget. *Nature Geoscience*, 11, 49–54. <https://doi.org/10.1038/s41561-017-0018-z>
- Nash, J. D., Alford, M. H., & Kunze, E. (2005). Estimating internal wave energy fluxes in the ocean. *Journal of Atmospheric and Oceanic Technology*, 22(10), 1551–1570. <https://doi.org/10.1175/JTECH1784.1>
- Nick, F. M., Vieli, A., Howat, I. M., & Joughin, I. (2009). Large-scale changes in Greenland outlet glacier dynamics triggered at the terminus. *Nature Geoscience*, 2(2), 110–114. <https://doi.org/10.1038/ngeo394>
- Nilsen, F., Skogseth, R., Vaardal-Lunde, J., & Inall, M. E. (2016). A simple shelf circulation model: Intrusion of Atlantic water on the West Spitsbergen Shelf. *Journal of Physical Oceanography*, 46(4), 1209–1230. <https://doi.org/10.1175/JPO-D-15-0058.1>
- Nøst, E. (1994). Calculating tidal current profiles from vertically integrated models near the critical latitude in the Barents Sea. *Journal of Geophysical Research*, 99(C4), 7885–7901.
- Oltmanns, M., Straneo, F., Moore, G. W., & Mernild, S. H. (2014). Strong downslope wind events in Ammassalik, Southeast Greenland. *Journal of Climate*, 27(3), 977–993. <https://doi.org/10.1175/JCLI-D-13-00067.1>
- Rignot, E., & Kanagaratnam, P. (2006). Changes in the velocity structure of the Greenland Ice Sheet. *Science*, 311(5763), 986–990. <https://doi.org/10.1126/science.1121381>

- Sciascia, R., Cenedese, C., Nicoli, D., Heimbach, P., & Straneo, F. (2014). Impact of periodic intermediary flows on submarine melting of a Greenland glacier. *Journal of Geophysical Research: Oceans*, 119, 7078–7098. <https://doi.org/10.1002/2014JC009953>
- Sciascia, R., Straneo, F., Cenedese, C., & Heimbach, P. (2013). Seasonal variability of submarine melt rate and circulation on an East Greenland fjord. *Journal of Geophysical Research: Oceans*, 118, 2492–2506. <https://doi.org/10.1002/jgrc.20142>
- Spall, M. A., Jackson, R. H., & Straneo, F. (2017). Katabatic wind-driven exchange in fjords. *Journal of Geophysical Research: Oceans*, 122, 8246–8262. <https://doi.org/10.1002/2017JC013026>
- Stigebrandt, A. (2012). Hydrodynamics and circulation of fjords. In L. Bengtsson, et al. (Eds.), *Encyclopedia of lakes and reservoirs*. Netherlands: Springer Science + Business Media B.V, pp. 327–344.
- Stokes, G. G. (1847). On the theory of oscillatory waves. *Transactions of the Cambridge Philosophical Society*, 8(8), 441–455. <https://doi.org/10.1017/CBO9780511702242.016>
- Støylen, E., & Weber, J. E. H. (2010). Mass transport induced by internal Kelvin waves beneath shore-fast ice. *Journal of Geophysical Research*, 115, C03022. <https://doi.org/10.1029/2009JC005298>
- Straneo, F., Hamilton, G. S., Sutherland, D. A., Stearns, L. A., Davidson, F., Hammill, M. O., et al. (2010). Rapid circulation of warm subtropical waters in a major glacial fjord in East Greenland. *Nature Geoscience*, 3(3), 182–186. <https://doi.org/10.1038/ngeo764>
- Straneo, F., Heimbach, P., Sergienko, O., Hamilton, G. S., Catania, G. A., Griffies, S., et al. (2013). Challenges to understanding the dynamic response of Greenland's marine terminating glaciers to oceanic and atmospheric forcing. *Bulletin of the American Meteorological Society*, 94(8), 1131–1144. <https://doi.org/10.1175/BAMS-D-12-00100.1>
- Sutherland, D. A., Roth, G. E., Hamilton, G., Mernild, S. H., Stearns, L. A., & Straneo, F. (2014). Quantifying flow regimes in a Greenland glacial fjord using iceberg drifters. *Geophysical Research Letters*, 41, 8411–8420. <https://doi.org/10.1002/2014GL062256>
- Sutherland, D. A., & Straneo, F. (2012). Estimating ocean heat transports and submarine melt rates in Sermilik fjord, Greenland, using lowered acoustic doppler current profiler (LADCP) velocity profiles. *Annals of Glaciology*, 53(60), 50–58. <https://doi.org/10.3189/2012AoG60A050>
- Sutherland, D. A., Straneo, F., & Pickart, R. S. (2014). Characteristics and dynamics of two major Greenland glacial fjords. *Journal of Geophysical Research: Oceans*, 119, 3767–3791. <https://doi.org/10.1002/2013JC009786>
- Torrence, C., & Compo, G. P. (1998). A practical guide to wavelet analysis. *Bulletin of the American Meteorological Society*, 79(1), 61–78. [https://doi.org/10.1175/1520-0477\(1998\)079<0061:APGTWA>2.0.CO;2](https://doi.org/10.1175/1520-0477(1998)079<0061:APGTWA>2.0.CO;2)
- Treasure, A., Roquet, F., Ansorge, I., Bester, M., Boehme, L., Bornemann, H., et al. (2017). Marine mammals exploring the oceans pole to pole: A review of the MEOP Consortium. *Oceanography*, 30(2), 132–138. <https://doi.org/10.5670/oceanog.2017.234>
- Wunsch, C. (1973). On the mean drift in large lakes. *Limnology and Oceanography*, 18, 793–794. <https://doi.org/10.4319/lo.1973.18.5.0793>
- Young, W. R., Rhines, P. B., & Garrett, C. J. R. (1982). Shear-flow dispersion, internal waves and horizontal mixing in the ocean. *Journal of Physical Oceanography*, 12(6), 515–527. [https://doi.org/10.1175/1520-0485\(1982\)012<0515:SFDIWA>2.0.CO;2](https://doi.org/10.1175/1520-0485(1982)012<0515:SFDIWA>2.0.CO;2)